Vol.44 No.5　2020

Journal

広告　◇東英工業株式会社

JOURNAL OF THE MAGNETICS SOCIETY OF JAPAN

*Vol.*44 *No.*5 **2020**

日本磁気学会

HP: http://www.magnetics.jp/   e-mail: msj@bj.wakwak.com
Electronic Journal: http://www.jstage.jst.go.jp/browse/msjmag
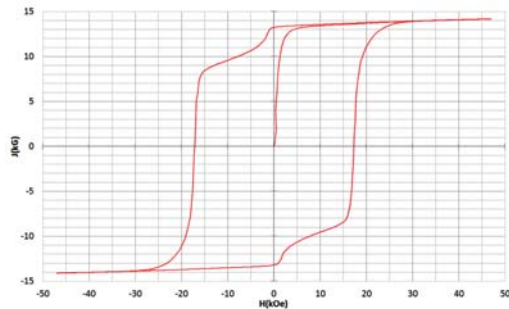
TOEI

世界初！
高温超電導型VSM

新製品

世界初*、高温超電導マグネットをVSMに採用することで
測定速度 当社従来機1/20を実現。
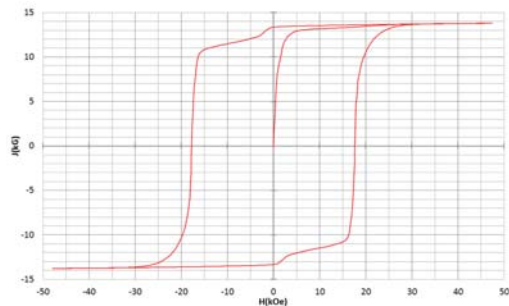0.5mm cube磁石のBr, HcJ高精度測定が可能と
なりました。
*2014年7月 東英工業調べ

測定結果例

高温超電導VSMによるNdFeB（sint.）0.5mm cube BHカーブ

磁化測定レンジ：0.2emu
Br = 13.2kG　　　　HcJ = 17.2kOe

高温超電導VSMによるNdFeB（sint.）1mm cube BHカーブ

磁化測定レンジ：2emu
Br = 13.3kG　　　　HcJ = 17.7kOe

高温超電導VSMによるNdFeB（sint.）4mm cube BHカーブ
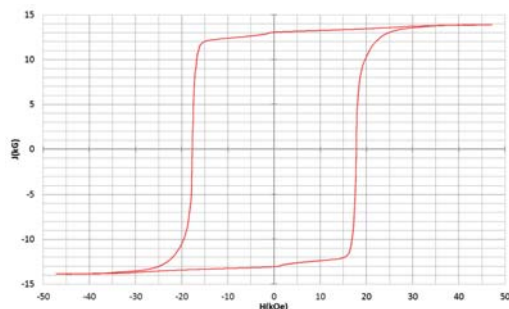
磁化測定レンジ：100emu
Br = 13.1kG　　　　HcJ = 17.8kOe

高速測定を実現

高温超電導マグネット採用により、高速測定を
実現しました。Hmax＝5Tesla, Full Loop測定が
2分で可能です。
（当社従来機：Full Loop測定 40分）

小試料のBr,HcJ高精度測定

0.5mm cube磁石のBr,HcJ高精度測定ができ、
表面改質領域を切り出しBr,HcJの強度分布等、
微小変化量の比較測定が可能です。
また、試料の加工劣化の比較測定が可能です。

試料温度可変測定

－50℃～＋200℃温度可変UNIT（オプション）

磁界発生部の小型化

マグネットシステム部寸法：0.8m×0.3m×0.3m

Journal of the Magnetics Society of Japan
Vol. 44, No. 5

CONTENTS

<Review>

Magneto-optical Imaging Using Bismuth-substituted Iron Garnet Films Prepared by Metal–Organic Decomposition

Takayuki Ishibashi

Nagaoka University of Technology, *1603-1 Kamitomioka, Nagaoka, Niigata 940-2188, Japan*

Magneto-optical (MO) imaging using an MO material is one of the most important imaging techniques for measuring magnetic field distributions. The technique is attracting attention because of its ability to visualize magnetic fields and current distributions at a wide range of temperatures from cryogenic to room temperature or higher, a wide range of length scales from micrometers to several tens of centimeters, and a wide range of frequencies from DC to GHz. Nevertheless, further development of films with good MO properties is required in order to extend the range of applications of MO imaging. In this paper, developments related to bismuth-substituted iron garnet films, $R_{3-x}Bi_xFe_{5-y}Ga_yO_{12}$ (R= Y, Nd; $1 \leq x \leq 3$), prepared by metal–organic decomposition for MO imaging plates are reviewed. In addition, an MO imaging plate with an electroluminescent backlight, which enables wide-area MO imaging, and the MO color imaging technique, which indicates the strength of a magnetic field using colors, are reviewed.

Key words: magneto-optical imaging, Faraday effect, Bi-substituted iron garnet, metal-organic decomposition

1. Introduction

Magneto-optical (MO) imaging has played an important role in both basic research on magnetic materials and applications such as magnetic recording technologies. The polarizing microscope developed in the 1950s has been used to visualize magnetic domains in magnetic materials via MO effects[1]. Magnetic domains become visible under a polarizing microscope because the polarization plane of the light from a sample is rotated as a result of the MO Kerr effect[2] in reflection or the Faraday effect[3] in transmission.

MO imaging techniques that utilize an MO material measure the magnetic field distribution in a magnetic material, whereas the aforementioned MO microscopy technique measures the magnetization. We refer to the plate with MO materials that enable visualization of magnetic fields as an MO imaging plate. The magnetic field distribution at a location on the MO imaging plate is visualized in real-time using the Faraday effect of the MO materials, as shown in Fig. 1. The MO imaging plates consist of an MO material (typically a bismuth (Bi)-substituted iron garnet film prepared on a transparent substrate as described below), a mirror layer, and a protection layer. The spatial resolution in MO imaging can be as high as the optical diffraction limit, although it is adversely affected by the dispersive characteristics of the magnetic field. However, MO imaging would enable the measurement samples with a large area (larger than several tens of square centimeters) if large MO imaging plates become available. Given these features, MO imaging is promising as a nondestructive measurement technique for characterizing electronic devices, detecting impurities and defects in metals. Moreover, it is considered a promising technique for characterizing magnetic fields with frequencies as high as the microwave range[4],[5].

2. MO imaging using Bi-substituted iron garnet

Alers introduced the MO imaging technique using paramagnetic cerium phosphate glass in 1959 to study the intermediate state in superconductors. The glass was later replaced by Eu-chalcogenides such as EuSe or EuS, which were used in a narrow temperature range in which both a large Faraday rotation angle and paramagnetism were utilized[6],[7]. MO imaging techniques using Bi-substituted iron garnets were first reported in 1989[8]. This approach enables the measurement of magnetic fields in a wide temperature range (from extremely low temperatures to a high temperature of ~100°C) using MO imaging[9],[10]. In the early stages of the development of MO imaging, the magnetic domain size in garnet films with perpendicular magnetic anisotropy limited the spatial resolution to the lengths of the magnetic domains. The use of Bi-substituted iron garnet, which exhibits in-plane magnetization, has led to a substantial improvement of the spatial resolution[11]. Consequently, the real-time observation of single vortices in superconductors has been realized[12]–[14].

The magnetic garnets have a garnet structure with cubic space group *Ia*3*d*. Their structure includes three tetrahedral and two octahedral sites for Fe^{3+} ions and three dodecahedral sites for R^{3+} rare-earth ions in one unit cell described by the chemical formula $R_3Fe_5O_{12}$. Each of the Fe^{3+} ions in the two sites has a magnetic moment of 5 μ_B with directions opposite to each other, resulting in a ferrimagnet with a relatively weak spontaneous magnetization. Most magnetic garnets have similar Curie temperatures of approximately 550 K, although some rare-earth elements have a magnetic moment induced by the moment of Fe^{3+}, aligned parallel or antiparallel to it depending on the rare-earth element. For MO imaging, yttrium or lutetium iron garnets have been used because Y^{3+} and Lu^{3+} do not have magnetic

(a)

Imaging device

Analyzer

θ

$\vec{E}$

Light

Beam splitter

Polarizer

Magnetization $\vec{M}$

$\vec{H}$

MO imaging plate

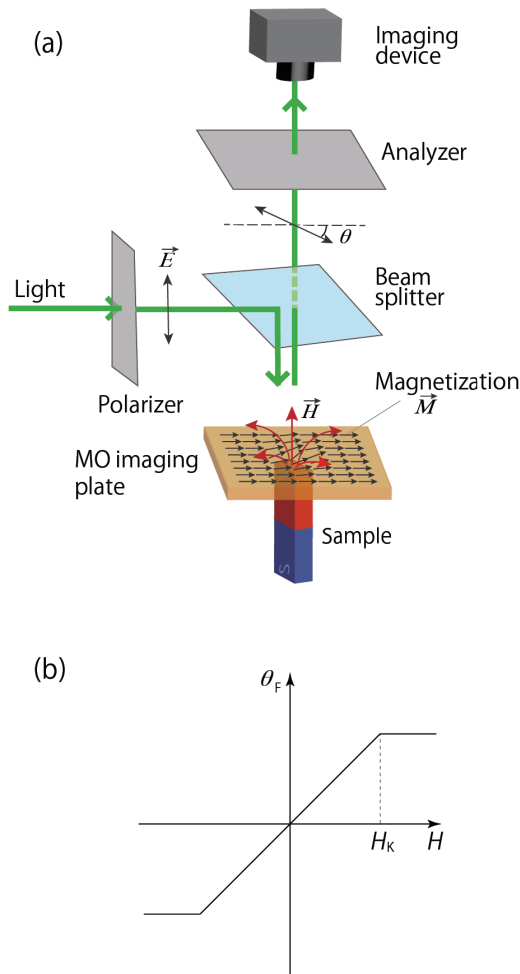Sample

(b)

θ_F

H_K H

Fig. 1 (a) A schematic of MO imaging using an MO imaging plate and (b) the magnetic-field dependence of the Faraday rotation of the MO imaging plate.

moments and, consequently, there is no magnetic compensation temperature and less temperature dependence of the magnetizations.

One of the most important properties of Bi-substituted iron garnets is their excellent MO properties, which can be improved by substituting Bi^{3+} for R^{3+}. The Faraday rotation for $Y_{3-x}Bi_xFe_5O_{12}$ (Bi:YIG) increases from 4°/μm for $x = 1$ to 30°/μm for $x = 3$ ($Bi_3Fe_5O_{12}$)[15]–[17]. Because of their excellent MO properties, Bi-substituted iron garnets have been used in various MO applications, including optical isolators[18], spatial light modulators[19],[20], and MO imaging plates. Moreover, they are promising materials for studying fast magnetization reversals using a femtosecond laser[21], spin-wave phenomena[22]–[24], the spin Seebeck effect[25]–[27], and terahertz emission[28].

In addition to the large Faraday rotation, the magnetic anisotropy of an MO material must be controlled for MO imaging. In-plane magnetic anisotropy with a linear magnetic-field dependence of Faraday rotation is suitable for MO imaging. From the viewpoint of magnetocrystalline anisotropy, (001)- or (011)-orientated

epitaxial films prepared on $Gd_3Ga_5O_{12}$ (GGG) single crystals with a lattice constant of 1.2383 nm have been used as substrates. The saturation magnetic field was controlled by substituting nonmagnetic elements such as Ga and Al for Fe, resulting in a decrease in the demagnetization field. In addition, magnetostrictive effects, which are affected by the lattice matching and whose values differ with the kind of rare-earth element, must also be considered for controlling the magnetic anisotropy.

To obtain Bi-substituted iron garnet films with a large proportion of Bi ($1.5 \leq x \leq 3$), researchers have used a wide variety of film growth techniques capable of growing films under nonequilibrium conditions, including sputtering, pulsed laser deposition[29]–[31], ion-beam sputtering[29], and the sol–gel method[17],[32]. The resultant films, however, often included secondary phases or exhibited cracks. However, highly Bi-substituted iron garnet films suitable for optical applications have been successfully grown by metal–organic decomposition (MOD)[33],[34], as described in section 3.

3. Preparation of Bi-substituted iron garnet films by MOD

3.1 MOD method

MOD is a film-growth method for oxides and offers several advantages:
- The process is simple and does not require a vacuum system.
- Chemical composition can be precisely controlled.
- MOD solutions are uniform at the molecular level and stable for several years.
- It enables the easy preparation of large-scale films.

Figure 2 shows a typical MOD procedure consisting of spin-coating of a MOD solution (3000 rpm, 60 s), drying (100°C, 10–30 min), pre-annealing to decompose the organic materials (~400°C, 10–30 min), and annealing to induce crystallization (700°C, 3 h). All of these thermal treatments are performed in air. We used MOD solutions prepared by Kojundo Chemical Co., Ltd. in our study. The starting materials for the MOD solutions consist of
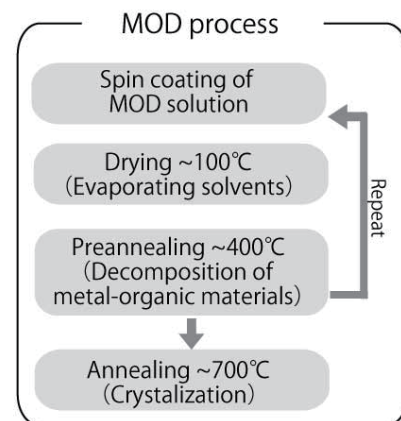
MOD process

Spin coating of MOD solution

Drying ~100°C (Evaporating solvents)

Preannealing ~400°C (Decomposition of metal-organic materials)

Repeat

Annealing ~700°C (Crystalization)

Fig. 2   A typical procedure in the MOD process.

solutions of metal octylates, including those of Bi, Y, Fe, Nd, and Ga. They are mixed to obtain the desired chemical proportion. The total concentration of octylates in the MOD liquids is usually fixed at 3–4%. The typical thickness of a single coated film is 30–40 nm.

3.2 Bi:YIG films

Figure 3 shows XRD patterns for $Y_{0.5}Bi_{2.5}Fe_5O_{12}$ (Bi2.5:YIG) and $Bi_3Fe_5O_{12}$ (BIG) films prepared on GGG (001). Only the 004 and 008 peaks are observed to the left of the peaks for the GGG substrate for both the YBIG and the BIG film, indicating that the Bi2.5:YIG and BIG films were both grown along the [100] direction. However, the films exhibited a granular structure consisting of grains smaller than 100 nm. Fortunately, because their magnetic domains are as small as their grains, these materials are suitable as materials for MO imaging in which the spatial resolution is limited by the magnetic domain structure. In fact, large zigzag domain structures, which have been observed in garnet films grown by the liquid-phase epitaxy, have not been observed in MOD-grown garnet films.

Figure 4 shows the magnetic-field dependence of the Faraday rotation for Bi:YIG films with $1.5 \leq x \leq 3$ on
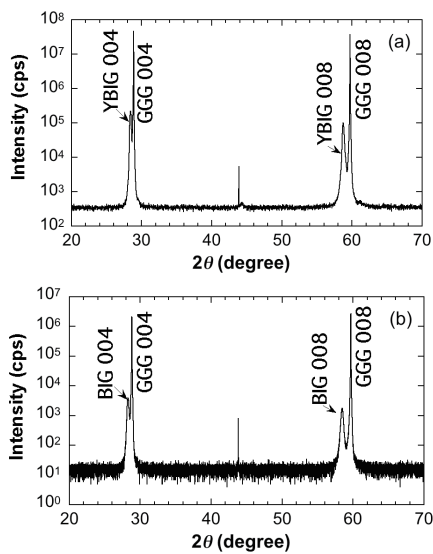
GGG(001) substrates, measured at a photon energy of 3 eV. A linear magnetic-field dependence of the Faraday rotation is observed below the saturation field of approximately 2 kOe for all of the samples represented in the figure.

Moreover, off-diagonal components of permittivity tensors were obtained[35] for the first time, as shown in Fig. 5. The permittivity tensor $\tilde{\varepsilon}$ was defined as

$$\tilde{\varepsilon} = \begin{bmatrix} \varepsilon_1 & -i \cdot \varepsilon_2 & 0 \\ i \cdot \varepsilon_2 & \varepsilon_1 & 0 \\ 0 & 0 & \varepsilon_3 \end{bmatrix}. \qquad (1)$$

These results indicate that Bi:YIG films prepared by the MOD method exhibited excellent MO properties and sufficient optical quality for optical analysis using ellipsometry.

3.3 Bi:NIG on GGG

As previously mentioned, Y^{3+} or Lu^{3+}, which have relatively small ionic radii, have been used in Bi-substituted iron garnets to minimize lattice mismatch between the garnet films and the GGG substrates. However, other rare-earth elements could be used if lattice matching is not required. In one study, Nd^{3+} was chosen because its ionic radius is similar to that of Bi^{3+} and its magnetic moment is parallel to the net magnetic moment of Fe^{3+} in garnets, and $Nd_{0.5}Bi_{2.5}Fe_{5-y}Ga_yO_{12}$ (Bi2.5Ga:NIG) films were successfully prepared by MOD[36),37]. Figure 6 shows magnetization curves of Bi2.5Ga:NIG films prepared on GGG(001) substrates,

Fig. 3 XRD patterns for (a) B2.5:YIG and (b) BIG films prepared on GGG(100) substrates.
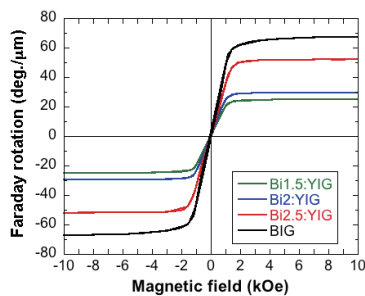
Fig. 4 Faraday rotation hysteresis loops of $Y_{3-x}Bi_xFe_5O_{12}$ films on GGG substrates, as measured at 3 eV.[35]
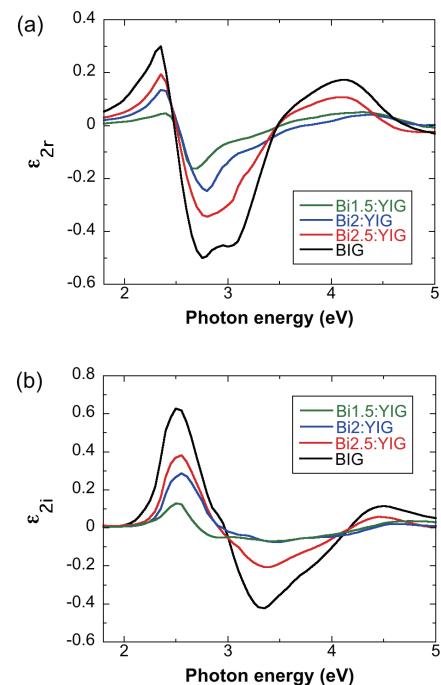

Fig. 5 (a) Real and (b) imaginary parts of off-diagonal elements of the permittivity tensor for $Y_{3-x}Bi_xFe_5O_{12}$ (x = 1.5, 2, 2.5, 3.0) prepared on GGG(001) substrates [35].
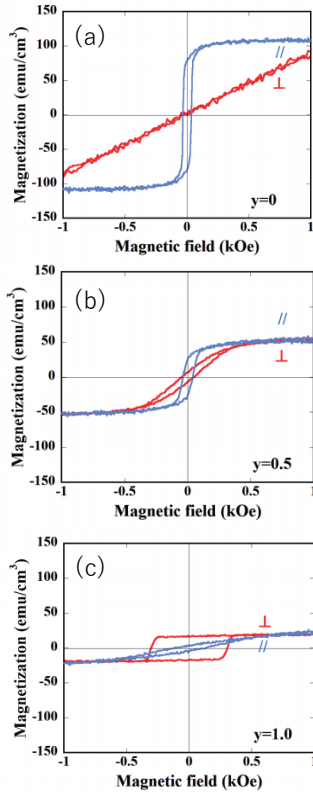
Fig. 6 Magnetization curves for $Nd_{0.5}Bi_{2.5}Fe_{5-y}Ga_yO_{12}$ films with (a) y = 0, (b) 0.5 and (c) 1.0 on GGG(001) substrates[36].
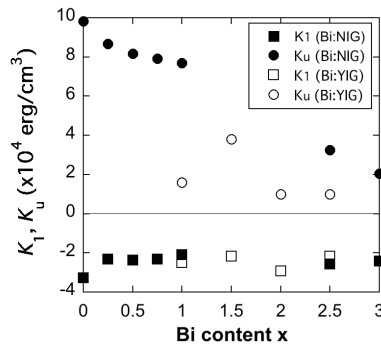
Fig. 7 Uniaxial magnetic anisotropy K_u and magnetocrystalline anisotropy K_1 in $Y_{3-x}Bi_xFe_5O_{12}$ and $Nd_{3-x}Bi_xFe_5O_{12}$ films.

showing that the magnetic anisotropy was controlled by substituting Ga^{3+} for Fe^{3+}. The effect of Nd^{3+} on the magnetic anisotropy was carefully analyzed using ferromagnetic resonance (FMR) measurements[37]. Figure 7 shows the uniaxial magnetic anisotropy K_u and magnetocrystalline anisotropy K_1 in Bi:YIG and Bi:NIG. The values of K_1 were found not to vary with the Bi content for either the Bi:YIG or the Bi:NIG films, and the value of K_u in Bi:YIG also did not varied with the Y content. By contrast, the value of K_u in Bi:NIG decreased

with decreasing Nd content, suggesting a large contribution of Nd^{3+} to the K_u. Aplesnin et al.[38] reported on the temperature dependence of the magnetostriction in Bi2.5:NIG films. They found a large temperature dependence of the magnetostriction effect in Bi2.5:NIG, indicating that the magnetic anisotropy could be varied with temperature.

3.4 Bi,Ga:NIG on glass substrate

Increasing the measurement area in MO imaging necessitated the development of highly Bi-substituted iron garnet films on glass substrates. However, the crystallization of highly Bi-substituted iron garnets with Bi contents in the range $2 \leq x \leq 3$, which are metastable materials, was found to be difficult on glass substrates. Okuda successfully grew a polycrystalline BIG film on a polycrystalline GGG layer prepared on a fused-quartz substrate at annealing temperatures ranging from 700 to 800°C. However, some secondary phases existed and the annealing temperature was too high for general glass substrates. Meanwhile, our group successfully prepared polycrystalline BIG films on Bi1:YIG buffer layers[39] and Bi2.5Ga:NIG on Bi1:NIG buffer layers[40),41)]. These films were prepared at annealing temperatures of 600–700°C[42], which were sufficiently low to enable the use of glass substrates. A photograph of a Bi2.5:NIG film prepared on a glass substrate (Eagle XG, Corning) with
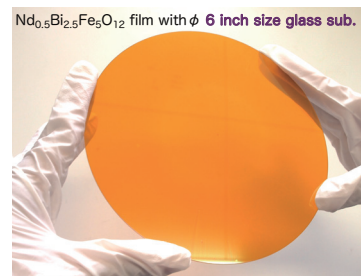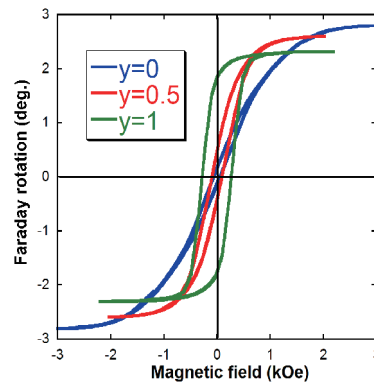

Fig. 8 Photo of a ⌀6 inch Bi2.5NIG film.

Fig. 9 Faraday hysteresis loops for $Nd_{0.5}Bi_{2.5}Fe_{5-y}Ga_yO_{12}$ films with y = 0, 0.5 and 1 and a thickness of 450 nm prepared on glass substrates.

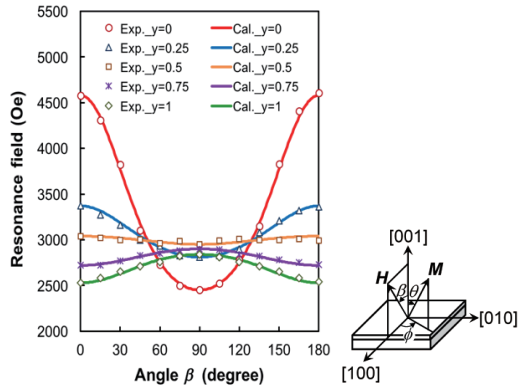**Fig. 10** Polar angle dependence of the FMR field for $Nd_{0.5}Bi_{2.5}Fe_{5-y}Ga_yO_{12}$ thin films on glass substrates.
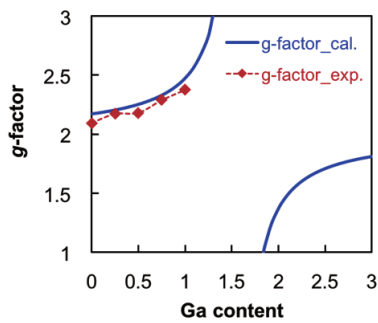

Fig. 12 Frequency dependence of MO signals for $Nd_{0.5}Bi_{2.5}Fe_{5-y}Ga_yO_{12}$ thin films on glass substrates with y = 0, 0.25, 0.5, 0.75 and 1 and Bi1:YIG on GGG (111) substrate.

Fig. 11 The g-factor of $Nd_{0.5}Bi_{2.5}Fe_{5-y}Ga_yO_{12}$ thin films with y = 0, 0.25, 0.5, 0.75 and 1 prepared on glass substrates.

a diameter of 6 inches is shown in Fig. 8.

The Bi2.5Ga:NIG films exhibited Faraday rotation angles comparable to those for films on single-crystalline GGG substrates, and the magnetic anisotropy was controlled by substituting Ga^{3+} for Fe^{3+}, as shown in Fig. 9[43].

Magnetic anisotropy and high-frequency properties have been studied by FMR measurements[44]. The resonant magnetic field H_{res} measured for X-band (9.09 GHz) microwaves is plotted as a function of the polar angle β in Fig. 10 with the coordinate system used in the FMR experiment. Open circles represent the experimental data, and solid lines indicate fitted data using the equation[45]

$$\left(\frac{\omega}{\gamma}\right)^2 = \left[H_{res}\cos(\beta-\theta) + 2\left(\frac{K_u}{M_s} - 2\pi M_s\right)\cos 2\theta\right]$$
$$\times \left[H_{res}\cos(\beta-\theta) + 2\left(\frac{K_u}{M_s} - 2\pi M_s\right)\cos^2\theta\right], \quad (2)$$

where ω is the angular frequency of the microwaves, θ is the angle between M and the [001] direction, and M_s is the saturation magnetization. K_u and the gyromagnetic ratio γ were estimated by fitting the β dependence of H_{res}. The K_u values obtained in this analysis were
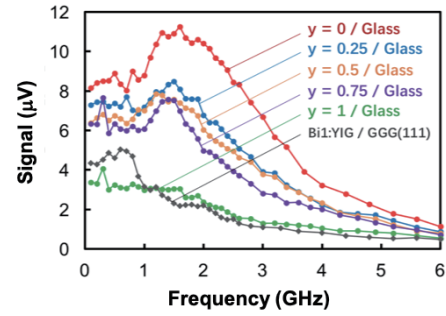
approximately the same as those measured via torque measurements[41]. The g-factor values were obtained using the equation, $g = \gamma h/2\pi\mu_B$, where μ_B is the Bohr magneton and h is Planck's constant, and are plotted as a function of the Ga content in Fig. 11. The g-factor slightly increased with increasing Ga content. This behavior can be explained by the existence of the orbital angular momentum μ_{orb} in Nd^{3+} in addition to the spin moment μ_{spin}, as given[46] by

$$g = 2\left(1 + \frac{\mu_{orb}}{\mu_{spin}}\right). \quad (3)$$

Similar behavior of the g-factor around the compensation point has been reported for $Eu_3Fe_{5-x}Ga_xO_{12}$, although the sign of the μ_{spin} was opposite to that in this case because the direction of the magnetic moment in Eu^{3+} was opposite to that in Nd^{3+}. From the viewpoint of the magnetic moment of each ion, the effective gyromagnetic ratio γ_{eff} is expressed[47] by

$$\gamma_{eff} = \frac{M_{Nd} + (M_{Fe}(tet.) - M_{Fe}(oct.))}{\dfrac{M_{Nd}}{|\gamma_{Nd}|} + \dfrac{M_{Fe}(tet.) - M_{Fe}(oct.)}{|\gamma_{Fe}|}}, \quad (4)$$

where M_{Nd} is the magnetic moment of Nd^{3+}, $M_{Fe}(tet.)$ and $M_{Fe}(oct.)$ are the magnetic moments of Fe^{3+} in tetrahedral and octahedral sites, respectively, and γ_{Nd} and γ_{Fe} are the gyromagnetic ratios of the rare-earth sublattice and net Fe^{3+}-ion sublattice, respectively. The decrease of the g-factor with increasing Ga content is explained by the decrease of the net magnetic moment $M_{Fe}(tet.) - M_{Fe}(oct.)$ with increasing Ga substitution. These results are consistent with the magnetic moment of the Nd^{3+} ions being parallel to the net magnetic moment of the Fe^{3+} ions, and indicate that the Nd^{3+} ions play an important role in determining magnetic properties such as the γ_{eff} even though the Nd content was as low as 0.5. Because of the larger γ_{eff}, the magnetization in Bi,Ga:NIG could respond at higher

frequencies.

MO signals measured at high frequencies using Bi2.5Ga:NIG films on glass substrates are shown in Fig. 12. The AC magnetic field induced by the AC current with frequencies as high as 6 GHz was measured at the edge of a microstrip line by the stroboscopic method using short laser pulses without a bias magnetic field[48),49)]. Figure 12 shows signal voltages corresponding to MO responses measured using Bi2.5Ga:NIG films with a Ga content $0 \leq y \leq 1$ on glass substrates. For comparison, the result for a Bi1:YIG thin film on a GGG(111) substrate prepared by MOD is also shown. It should be noted that these samples were measured with the same condition. MO signals were detected at frequencies as high as 6 GHz for all of the Bi2.5Ga:NIG thin films, and they had broad resonance peaks between 1.5 and 2 GHz. By contrast, the MO signal measured using a Bi:LIG film grown by the LPE method showed a sharp resonance peak[49)].

4. MO imaging using Bi-substituted iron garnet films prepared by MOD

4.1 MO imaging using Bi:YIG on GGG(001)

Figure 13 shows MO images of magnetic recording marks in videotapes measured using a Bi2.5:YIG film with a thickness of 200 nm[34)]. The wavelengths of the measured recording marks in Fig. 13(a) and 13(b) were 4 and 1.16 μm, respectively. Zigzag-shaped magnetic domains recorded in the videotapes were clearly observed. This result indicates that the spatial resolution in MO imaging using the Bi2.5:YIG film is better than 0.6 μm, which is sufficient for measurements using an optical microscope. One of the advantages of highly Bi-substituted iron garnet is its high submicron-scale spatial resolution, which is achieved by a submicron-thick film with a large Faraday rotation angle.

4.2 MO imaging plate combined with backlight

An optical setup with extraordinarily large lenses and a half-mirror will be required to achieve sufficiently uniform polarization over a large area. To solve this problem, Nagakubo et al. have proposed combining an MO imaging plate with a thin electroluminescent (EL) backlight and a linear polarizing film, as shown in Fig.
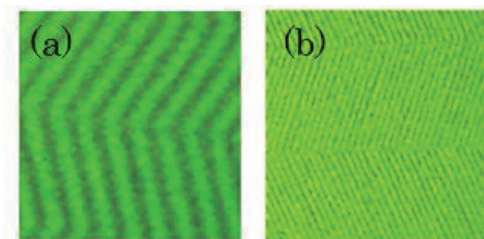
14. A camera and an analyzer were used to acquire the MO signals[50)]. In addition, a quarter-wave plate was placed in front of the analyzer for quantitative measurement. Figure 15 shows the magnetic field distribution for a smart phone. The magnetic field distribution from permanent magnets used in the camera, speakers, and the taptic device were clearly observed.

The magnetic field distributions were quantitatively obtained by measuring the MO effect, rotation angle θ, or ellipticity η using equations[50),51)]

$$\theta \approx \frac{2I_{LP} - (I_{RCP} + I_{LCP})}{2(I_{RCP} + I_{LCP})} \qquad (5)$$

$$\eta \approx \frac{I_{RCP} - I_{LCP}}{2(I_{RCP} + I_{LCP})} \qquad (6)$$

where I_{LP}, I_{RCP}, and I_{LCP} are the light intensities for linear and right- and left-circular polarization, respectively, measured at each pixel of the imaging sensor in the imaging device. Quantitative values of the magnetic field were obtained from the magnetic-field dependences of θ or η. An MO image of a stack of Nd magnets and the corresponding line profile are shown in Fig. 16. The validity of the measured values has been discussed[47)].
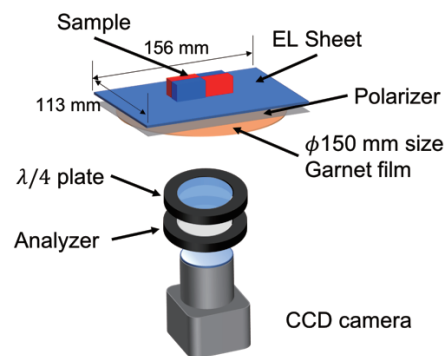

Fig. 14 An MO imaging setup with an MO imaging plate with a backlight.
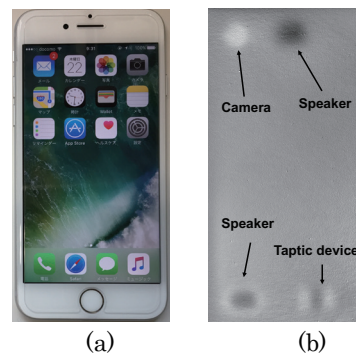

Fig. 15 (a) A Photograph of a smartphone and (b) its MO image.

Fig. 13 MO images of video tapes magnetically recorded with wavelengths of (a) 4 μm and (b) 1.16 μm, measured using a B2.5:YIG film on GGG(001) [34)].
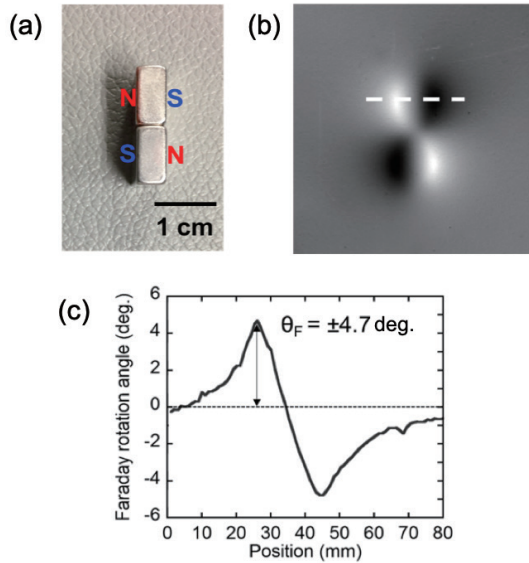
Fig. 16 (a) Digital photograph of Nd magnets; (b) MO image and (c) line profile corresponding to the white line.

4.3 MO color imaging

Spectral shapes of the Kerr rotation of the MO imaging plates measured in reflection geometry are influenced by light interference. Consequently, they differ from their original spectral structures, resulting in MO images that could become colorful. For example, the Kerr rotation spectrum of an MO imaging plate using Bi2:NIG with a thickness of 450 nm is shown in Fig. 17. Peaks are observed at wavelengths of 530 and 595 nm, corresponding to green and yellow, respectively. By varying the chemical composition and/or the thickness of the garnet film, or the light source, researchers could vary the color depending on the magnetic field as previously reported[42]. Figure 18 shows three results obtained experimentally using various light sources (i.e., a white LED, green and yellow LEDs, and blue and yellow LEDs) plotted in the chromaticity diagram (CIE1931), in which each curve indicates that color varies with the magnetic field strength. The magnetic field was quantitatively evaluated with colors expressed as RGB values. More details of the MO color imaging technique will be found in Ref. 42.

Figure 19 shows a demonstration of quantitative MO color imaging using a white LED and a commercial ferrite magnet. The color scale indicates the strength of the magnetic field. In the MO image, south (S) and north (N) magnetic poles are indicated by yellow and blue, respectively; the zero point is indicated by violet.

We expect the resolution of the displayed magnetic field to be improved through the use of a color instead of a monochrome display. Specifically, the resolution of the magnetic field in color can potentially be the cube of that in monochrome. For example, in the case of an 8-bit camera, magnetic field values could be expressed with
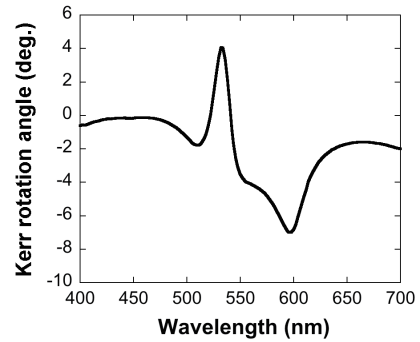

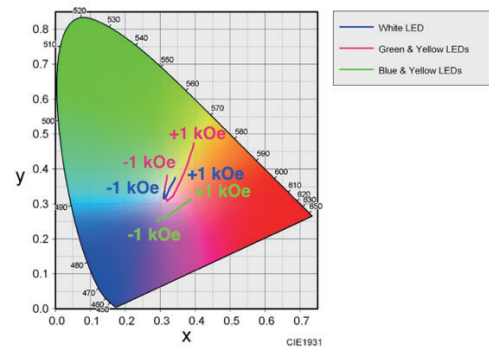**Fig. 17** Kerr spectrum of the Bi2:NIG film on a glass substrate.

Fig. 18 Color table showing the location of data experimentally obtained using white LEDs, green and yellow LEDs, and blue and yellow LEDs as light sources.
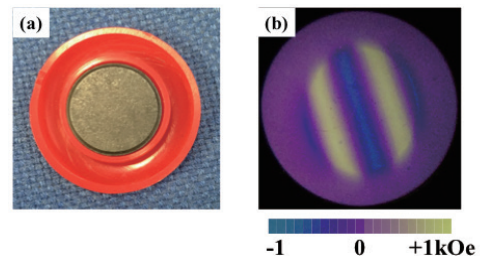
Fig. 19 (a) Digital photograph of a spherical magnet and (b) the corresponding MO color image

$2^{8 \times 3} = 16,777,216$ colors, compared with $2^8 = 256$ in monochrome.

5. Summary

An MO imaging technique using an MO imaging plate has been developed as a powerful method that visualizes the magnetic field distribution at a wide range of temperatures from cryogenic to greater than 100ºC, at length scales from micrometers to several tens of centimeters, and at frequencies from DC to GHz. The spatial and time resolutions have been improved through the use of Bi-substituted iron garnet films as MO imaging

plates. In this paper, Bi-substituted iron garnet films fabricated by the MOD method were reviewed, where highly Bi-substituted iron garnet films on glass substrates as well as on GGG substrates were discussed. In addition, an MO imaging plate with an EL backlight for wide-area MO imaging and for MO color imaging with high magnetic resolution were reviewed. Further advances in MO materials and measurement techniques are expected to broaden the application range of MO imaging.

References

1) J. McCord, *J. Phys. D. Appl. Phys.* **48**, 333001 (2015).

2) J. Kerr, *The London, Edinburgh, Dublin Philos. Mag. J. Sci.* **3** [19], 321 (1877).

3) Michael Faraday, *Philosophical Transactions of the Royal Society of London*, **136**, 1 (1846).

4) M. Takahashi, K. Kawasaki, H. Ohba, T. Ikenaga, H. Ota, T. Orikasa, N. Adachi, K. Ishiyama and K. I. Arai, *J. Appl. Phys.* **107** [9], 10 (2010).

5) E. Yamazaki, H. Park, S. Wakana, M. Kishi and M. Tsuchiya, *Jpn. J. Appl. Phys.*, Part 2 Lett. **41** [7 B], 3 (2002).

6) H. Kirchner, *Phys. Status Solidi* **4** [2], 531 (1971).

7) B. Dutoit and L. Rinderer, *Jpn. J. Appl. Phys.* **26** [S3-2], 1661 (1987).

8) A. A. Polyanskii, V. K. Vlasko-Vlasov, M. V. Indenbom and V. I. Nikitenko, *Sov. Tech. Phys. Lett.* **15**, 872 (1989).

9) M. V. Indenbom, N. N. Kolesnikov, M. P. Kulakov, I. G. Naumenko, V. I. Nikitenko, A. A. Polyanskii, N. F. Vershinin and V. K. Vlasko-Vlasov, *Phys. C Supercond.* **166** [5–6], 486 (1990).

10) S. Gotoh, N. Koshizuka, M. Yoshida, M. Murakami and S. Tanaka, *Jpn. J. Appl. Phys.* **29** [7], L1083 (1990).

11) L. A. Dorosinskii, M. V. Indenbom, V. I. Nikitenko, Y. A. Ossip'yan, A. A. Polyanskii and V. K. Vlasko-Vlasov, *Phys. C Supercond.* **203** [1–2], 149 (1992).

12) P. E. Goa, H. Hauglin, Å. A. F. Olsen, D. Shantsev and T. H. Johansen, *Appl. Phys. Lett.* **82** [1], 79 (2003).

13) P. E. Goa, H. Hauglin, Å. A. F. Olsen, M. Baziljevich and T. H. Johansen, *Rev. Sci. Instrum.* **74** [1 I], 141 (2003).

14) P. E. Goa, H. Hauglin, M. Baziljevich, E. Il'Yashenko, P. L. Gammel and T. H. Johansen, *Supercond. Sci. Technol.* **14** [9], 729 (2001).

15) L. E. Helseth, R. W. Hansen, E. I. Il'yashenko, M. Baziljevich and T. H. Johansen, *Phys. Rev. B* **64**.174406 (2001).

16) S. Wittekoek, T. J. A. Poprna, J. M. Robertson and P. F. Bongers, *Phys. Rev. B* **12** [7], 2777 (1975).

17) M. Gomi, K. Satoh and M. Abe, *J. Appl. Phys.* **63** [8], 3642 (1988).

18) T. Ishikawa, T. Masumoto, S. Ono and K. Sshiroki, *J. Magn. Soc. Japan* **11**, S1_353 (1987).

19) Y. Suzuki, T. Goto, Y. Eto, H. Takagi, P. B. Lim, A. V. Baryshev and M. Inoue, *J. Magn. Soc. Japan* **36** [3], 183 (2012).

20) H. N. Farhat and Z. Y. Shae, *Appl. Opt.* **28** [22], 4792 (1989).

21) F. Hansteen, A. Kimel, A. Kirilyuk and T. Rasing, *Phys. Rev. Lett.* **95** [4], 047402 (2005).

22) P. Khan, M. Kanamaru, W.-H. Hsu, M. Kichise, Y. Fujii, A. Koreeda and T. Satoh, *J. Phys. Condens. Matter* **31** [27], 275402 (2019).

23) Y. Hashimoto, T. H. Johansen and E. Saitoh, *Appl. Phys. Lett.* **112** [23], 232403 (2018).

24) Y. Hashimoto, T. H. Johansen and E. Saitoh, *Appl. Phys. Lett.* **112** [7], 072410 (2018).

25) A. Kirihara, K. I. Uchida, Y. Kajiwara, M. Ishida, Y. Nakamura, T. Manako, E. Saitoh and S. Yorozu, *Nat. Mater.* **11** [8], 686 (2012).

26) G. Siegel, M. C. Prestgard, S. Teng and A. Tiwari, *Sci. Rep.* **4**, 1 (2014).

27) H. Asada, A. Kuwahara, N. Sakata, T. Ono, T. Ishibashi, A. Meguro, T. Hashinaka, K. Kishimoto and T. Koyanagi, *J. Appl. Phys.* **117** [17], 17C724 (2015).

28) T. S. Seifert, S. Jaiswal, J. Barker, S. T. Weber, I. Razdolski, J. Cramer, O. Gueckstock, S. F. Maehrlein, L. Nadvornik, S. Watanabe, C. Ciccarelli, A. Melnikov, G. Jakob, M. Münzenberg, S. T. B. Goennenwein, G. Woltersdorf, B. Rethfeld, P. W. Brouwer, M. Wolf, M. Kläui and T. Kampfrath, *Nat. Commun.* **9** [1], 1 (2018).

29) N. Adachi, V. P. Denysenkov, S. I. Khartsev, A. M. Grishin and T. Okuda, *J. Appl. Phys.* **88** [5], 2734 (2000).

30) A. M. Grishin, S. I. Khartsev and S. Bonetti, *Appl. Phys. Lett.* **88** [24], 242504 (2006).

31) S. Kahl and A. M. Grishin, *J. Magn. Magn. Mater.* **278** [1–2], 244 (2004).

32) T. Okuda, N. Koshizuka, K. Hayashi, H. Taniguchi, K. Satoh and H. Yamamoto, *IEEE Transl. J. Magn.* Japan **3** [6], 483 (1988).

33) T. Ishibashi, A. Mizusawa, M. Nagai, S. Shimizu, K. Sato, N. Togashi, T. Mogi, M. Houchido, H. Sano and K. Kuriyama, *J. Appl. Phys.* **97** [1], 013516 (2005).

34) T. Kosaka, M. Naganuma, M. Aoyagi, T. Kobayasi, S. Niratisairak, T. Nomura and T. I. T. Ishibashi, *J. Magn. Soc.*

Japan **35** [3], 194 (2011).

35) E. Jesenska, T. Yoshida, K. Shinozaki, T. Ishibashi, L. Beran, M. Zahradnik, R. Antos, M. Kučera and M. Veis, *Opt. Mater. Express* **6** [6], 1986 (2016).

36) M. Sasaki, G. Lou, Q. Liu, M. Ninomiya, T. Kato, S. Iwata and T. Ishibashi, *Jpn. J. Appl. Phys.* **55** [5], 055501 (2016).

37) J. Yamakita, G. Lou, M. Nishikawa, T. Kato, S. Iwata and T. Ishibashi, *Jpn. J. Appl. Phys.* **57** [9S2], 09TC01 (2018).

38) S. S. Aplesnin, A. N. Masyugin, M. N. Sitnicov, U. I. Rybina and T. Ishibashi, *J. Magn. Magn. Mater.* **464**, 44 (2018).

39) S. Ikehara, K. Wada, T. Kobayashi, S. Goto, T. Yoshida, T. Ishibashi and T. Nishi, *J. Magn. Soc. Japan* **36** [3], 169 (2012).

40) T. Yoshida, K. Oishi, T. Nishi and T. Ishibashi, in *EPJ Web of Conferences* (2014) Vol. 75.

41) G. Lou, T. Kato, S. Iwata and T. Ishibashi, *Opt. Mater. Express* **7** [7], 2248 (2017).

42) Y. Nagakubo, Y. Baba, Q. Liu, G. Lou and T. Ishibashi, *J. Magn. Soc. Japan* **41**, 29 (2017).

43) G. Lou, T. Yoshida and T. Ishibashi, *J. Appl. Phys.* **117** [17], 17A749 (2015).

44) G. Lou, *Dotoral thesis, Nagaoka University of Technology* (2018).

45) H. Makino and Y. Hidaka, *Mater. Res. Bull.* **16** [8], 957 (1981).

46) C. Kittel, *Phys. Rev.* **76** [6], 743 (1949).

47) R. C. Lecraw, J. P. Remeika and H. Matthews, *Phys. Lett.* **12** [1], 9 (1964).

48) H. Nasuno, S. Hashi and K. Ishiyama, *IEEE Trans. Magn.* **47** [10], 4011 (2011).

49) N. Adachi, D. Uematsu, T. Ota, M. Takahashi, K. Ishiyama, K. Kawasaki, H. Ota, K. Arai, S. Fujisawa, S. Okubo and H. Ohta, *IEEE Trans. Magn.* **46** [6], 1986 (2010).

50) Y. Nagakubo, M. Sasaki, S. Meguro, M. Nishikawa and T. Ishibashi, *Jpn. J. Appl. Phys.* **57** [9S2], 09TC02 (2018).

51) T. Ishibashi, Z. Kuang, S. Yufune, T. Kawata, M. Oda, T. Tani, Y. Iimura, K. Sato, Y. Konishi, K. Akahane, X. Zhao and T. Hasegawa, *J. Appl. Phys.* **100** [9], 093903 (6 pages) (2006).

<Paper>

MnGa Film with (001) Texture Fabricated on Thermally Oxidized Si Substrate Using CoGa Buffer Layer

Y. Miwa*, D. Oshima**, T. Kato*, and S. Iwata**

*Department of Electronics, Nagoya University, *Furo-cho, Chikusa-ku, Nagoya, 464-8603, Japan*

** Institute of Materials and Systems for Sustainability, *Furo-cho, Chikusa-ku, Nagoya, 464-8603, Japan*

(001)-oriented MnGa films were grown on thermally oxidized Si substrates using CoGa buffer layers by the magnetron sputtering method. The deposition and annealing temperatures of the CoGa buffer layer were optimized to improve (001)-orientation of the MnGa layer. As a result, a saturation magnetization of 290 emu/cc was obtained when CoGa was sputter-deposited at 400 ˚C and post-annealed at 700 ˚C. This saturation magnetization was almost equal to that of MnGa grown on an MgO(001) substrate. The (001)-oriented MnGa film grown on the Si substrate had surface roughness compared to that grown on MgO(001) due to the high temperature annealing of the CoGa layer. Improvement of surface flatness is necessary for applications to magnetic memory and storage such as magnetic tunnel junctions and bit patterned media.

Key words: MnGa, CoGa, magnetic recording, recording media, bit patterned media,

1. Introduction

The areal density of hard disk drive (HDD) is increasing every year, and further increase is desired. Energy-assisted magnetic recordings, such as heat- or microwave-assisted recordings, are under development to boost the areal density of HDD. These technologies will be followed by heated dot magnetic recording (HDMR), which combines heat- (or energy) assisted magnetic recording and bit patterned media (BPM) to extend the density more than 10 Tb/in^2 [1]. In BPM, bit boundaries are defined by a nano-fabrication technique, and low transition noise is obtained without sacrificing thermal stability compared to a conventional granular media[2]. In general, ion milling followed by trench filling with nonmagnetic materials between bits is used to define the bit boundary in BPM. However, there are several problems with this fabrication method of BPM, including rough surface of the media, large distribution of the switching field, and high fabrication cost. An alternative way to fabricate BPM is an ion irradiation technique, in which accelerated ions are irradiated to modify the magnetic properties locally without etching the media physically[3, 4]. Ion irradiation is a simple and cost-effective fabrication method, and no flattening process, such as trench filling, is required after the bit boundary has been defined.

In the early stages of the study of the ion irradiation method, Co/Pt[3-6] and Co/Pd[7-8] multilayer films with perpendicular magnetic anisotropies were used as media. The ion irradiation caused interdiffusion at the Co/Pt or Co/Pd interface, which lowers the perpendicular anisotropy and makes them in-plane magnetized films due to the demagnetizing energy. Thus, when these multilayers are used as ion irradiation BPM, perpendicularly magnetized bits are separated by the in-plane magnetized region, which causes exchange coupling between the bits, and limits the ultimate density of BPM. In order to avoid the exchange coupling, we focused on perpendicularly magnetized Cr- and Mn-based ordered alloy films, because their magnetism was varied from ferromagnetic to paramagnetic by ion irradiation through the change in their crystal structure from the ordered to the disordered phase[9-12]. In our previous work, we demonstrated dot-patterned MnGa films with a flat surface and low bit edge damage by 30 keV Kr$^+$ ion irradiation[12-13]. However, these results were obtained using MnGa grown on MgO(001) single crystal substrates, which are costly for practical application. Thus, we have studied the growth of (001)-textured L1$_0$-MnGa films on thermally oxidized Si substrates[14].

For the mass production of ion beam patterned BPM, resist masks are expected to be imprinted on the magnetic layer, and then accelerated ions are uniformly irradiated through these masks[15]. Thin (low-height) resist masks are generally required to reduce the pitch size of the patterning. However, when a thin resist mask is used, the energy of incident ions must be lowered to stop the incident ions by the resist masks / to protect the MnGa bit by the irradiation. On the other hand, the low-energy of ion irradiation requires a reduction in the thickness of MnGa films, because the penetration depth of incident ions depends on the ion energy.

The thickness of MnGa should be less than the penetration depth to kill the ferromagnetism of the "space" regions. Therefore, thin and uniform MnGa with large perpendicular anisotropy should be prepared on low-cost substrates for practical application. However, reducing the MnGa thickness is known to degrade the magnetic properties, such as squareness and increased coercivity[16]. Recently, Suzuki *et al.* reported that a CoGa buffer layer was effective for obtaining ultrathin MnGa films with a magnetic squareness close to unity[17]. In this study, we report the fabrication of ultrathin MnGa films on thermally oxidized Si substrates using

the CoGa buffer layer, and discuss the optimized growth conditions.

2. Experimental methods

The sample stack was Cr (2 nm) / MnGa (5 nm) / CoGa (0 or 30 nm) / Cr (20 nm) / MgO (20 nm) / CrB (5 nm) / NiTa (25 nm) / SiO$_2$ / Si substrate. An Ar$^+$ ion beam was used to clean the surface of the substrate. Most layers were deposited by RF magnetron sputtering, and only the MgO layer was deposited by e-beam evaporation. NiTa and CrB were inserted to obtain the (001)-oriented MgO buffer layer[17]. The sample was transferred between sputtering and e-beam evaporation chambers without breaking the vacuum to avoid contamination during the deposition of the Cr/MgO/CrB/NiTa buffer layer. The buffer layer was deposited at room temperature, and the sample was then annealed at 800 °C for 60 min. The CoGa layer was deposited at T_s^{CoGa} = 200–500 °C, and then annealed at T_a^{CoGa} = 500–800 °C for 30 min. The MnGa layer was deposited at 200 °C, and then annealed at 400 °C for 60 min. The Cr layer was sputter-deposited as a protective layer at a temperature lower than 150 °C. An epitaxial MnGa film on the MgO(001) si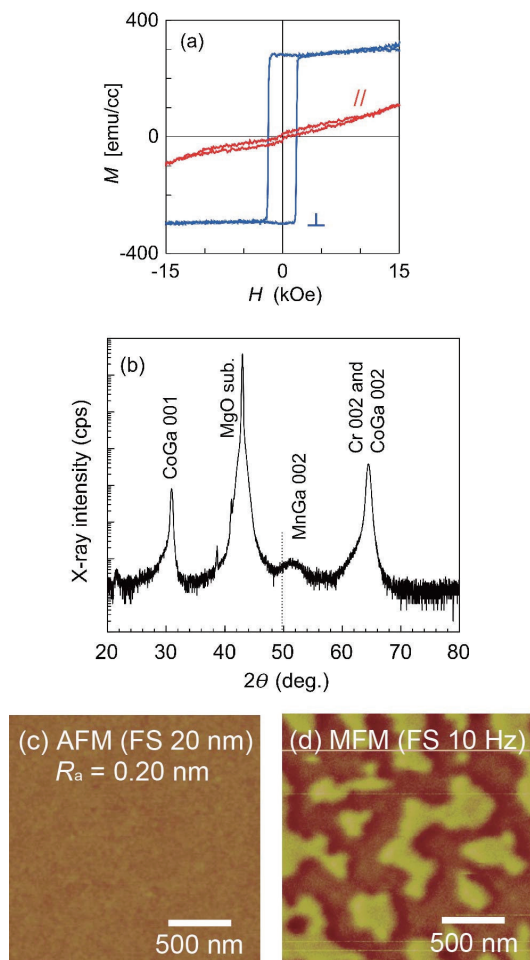ngle crystal substrate was also prepared as a reference. The MgO substrate was heated at 600 °C for 10 min before deposition. The structure was Cr (2 nm) / MnGa (5 nm) / CoGa (30 nm) / Cr (20 nm) / MgO(001) substrate. The growth temperatures were 400 °C, 400 °C, and 300 °C for the Cr, CoGa, and MnGa layers, respectively. The post-annealing was performed at 600 °C for 60 min, 400 °C for 30 min, and 400 °C for 60 min after the deposition of the Cr, CoGa, and MnGa layers, respectively. Finally, the protective Cr layer was deposited on the sample.

Magnetization curves were measured by an alternating gradient field magnetometer. Crystal structures were analyzed by X-ray diffraction (XRD) using Cu Kα radiation. Surface morphologies and magnetic domain structures were characterized by atomic force microscopy (AFM) and magnetic force microscopy (MFM) with a frequency mode, respectively.

3. Results and discussions

3.1 Ultrathin MnGa film grown on MgO substrate using CoGa buffer layer

Figure 1(a) shows the out-of-plane and in-plane M-H curves of the ultrathin MnGa film grown on the MgO substrate using a CoGa buffer layer. The out-of-plane curve showed a hysteresis with a squareness of unity; in contrast, the in-plane curve was almost linear with little hysteresis, showing a strong perpendicular anisotropy. The saturation magnetization M_s was ~ 300 emu/cc, which was smaller than thick MnGa films[12]. Figure 1(b) shows the XRD profile of the ultrathin MnGa film. CoGa 001, MnGa 002, Cr 002 and CoGa 002 peaks were observed, implying all the layers were epitaxially grown with (001)-orientation. The MnGa film had the L1$_0$-ordered phase from the fact that the ferromagnetism was observed as shown in Fig. 1 (a), however, MnGa 001 peak was not visible due to the thin MnGa layer. The peak position of MnGa 002 shifted to high angle side compared to the peak position of the bulk MnGa, implying lattice constant shrinks in the film normal and expands in the film. In addition, the peak shift for the ultrathin MnGa was larger than that for the thick MnGa
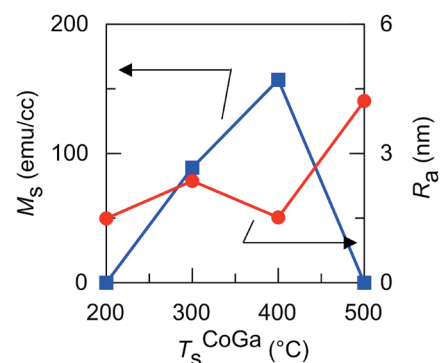

Fig. 1 (a) M-H curves, (b) XRD profile, (c) AFM, and (d) MFM images of ultrathin MnGa film on MgO substrate using CoGa buffer layer. Full scales (FS) of the images are (b) 20 nm and (c) 10 Hz.

Fig. 2 Saturation magnetization M_s and average roughness R_a of ultrathin MnGa films on Si substrates using CoGa buffer layers as a function of growth temperature T_s^{CoGa} of CoGa layer.

Fig. 4 Saturation magnetization M_s and average roughness R_a of ultrathin MnGa films on Si substrates using CoGa buffer layers as a function of annealing temperature T_a^{CoGa} for the CoGa layer.
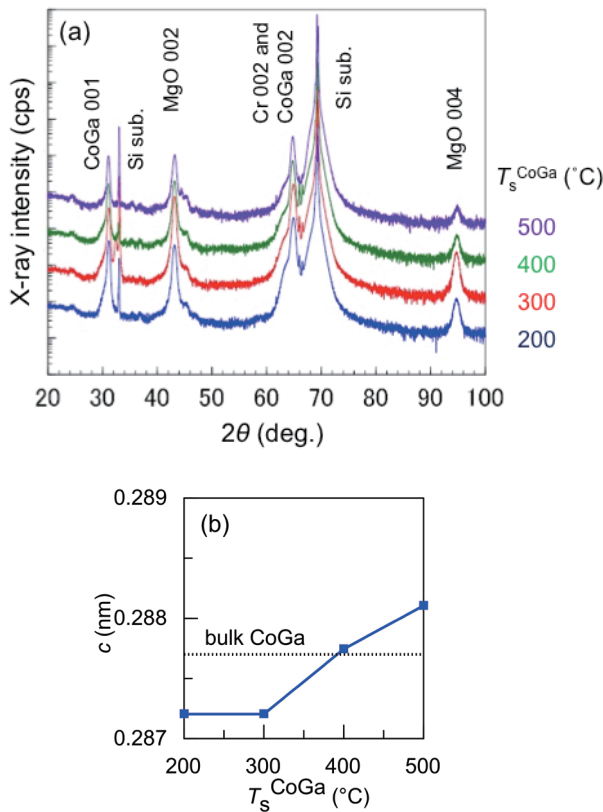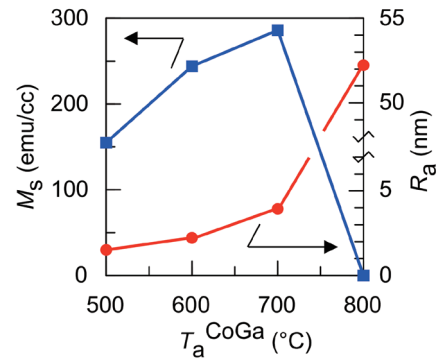

Fig. 3 (a) XRD patterns of ultrathin MnGa films on Si substrates using CoGa buffer layers. The growth temperature of CoGa T_s^{CoGa} was varied from 200–500 ˚C. (b) Lattice constant c of CoGa as a function of T_s^{CoGa}. The dashed line shows the value of bulk CoGa.
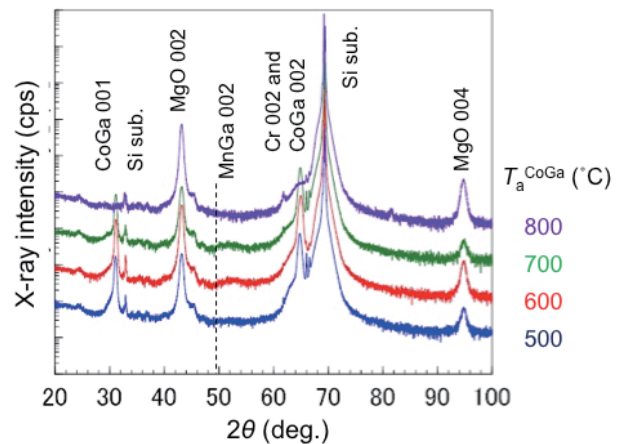

Fig. 5 XRD patterns of ultrathin MnGa films on Si substrates using CoGa buffer layers. The annealing temperature of CoGa T_a^{CoGa} was varied from 500–800 ˚C. The dashed line shows the peak positions of the bulk MnGa.

with M_s = 450 emu/cc[12] (not shown here). Accordingly, possible reasons for the small M_s of the thin MnGa films are low degree of $L1_0$ ordering and lattice distortion. Figures 1(c) and (d) show AFM and MFM images of the ultrathin MnGa film, respectively, grown on the MgO substrate using the CoGa buffer layer. Average roughness R_a estimated from the AFM image was 0.2 nm. In the MFM image, bright and dark regions were observed, which reflects the maze-like domain structure commonly seen in perpendicularly magnetized film. These results show that an ultrathin MnGa film with perpendicular anisotropy and flat surface was grown on the MgO substrate similarly to the results in our previous study[14].

3.2 Ultrathin MnGa (001)-oriented polycrystalline films grown on Si substrates using CoGa buffer layer

Details regarding the growth and annealing conditions of the seed layers underneath the CoGa layer are provided in our previous study[13]. In this paper, growth conditions for the CoGa layer were investigated to obtain high-quality ultrathin MnGa films. Figure 2 shows T_s^{CoGa} dependence of the M_s and R_a of ultrathin

MnGa films on Si substrates, where the CoGa buffer layer was post-annealed at T_a^{CoGa} = 500 ˚C. M_s was estimated from the hysteresis loop along the film normal direction, because the MnGa films were hard to saturate along the in-plane direction. When T_s^{CoGa} = 300 ˚C and 400 ˚C, the MnGa films showed perpendicular anisotropy. As shown in Fig. 2, large M_s and small R_a were obtained at T_s^{CoGa} = 400 ˚C. The M_s shown in Fig. 2 is considered to be sensitive to chemical ordering, lattice distortion, and (001)-orientation of the MnGa film. However, X-ray diffraction does not give us a clear answer for the variation of M_s, because MnGa 001 and 002 peaks were not visible, as shown in Fig. 3(a), due to the thin MnGa layer. Figure 3(a) shows the XRD patterns of ultrathin MnGa films on Si substrates using CoGa buffer layers, where the CoGa layer was deposited at T_s^{CoGa} = 200–500 ˚C and post-annealed at T_a^{CoGa} = 500 ˚C. CoGa 001 and 002, Cr 002, and MgO 002 and 004 peaks were observed for all the samples. This means that the CoGa, Cr, and MgO layers were all grown with (001)-orientation. Figure 3(b) shows the T_s^{CoGa}
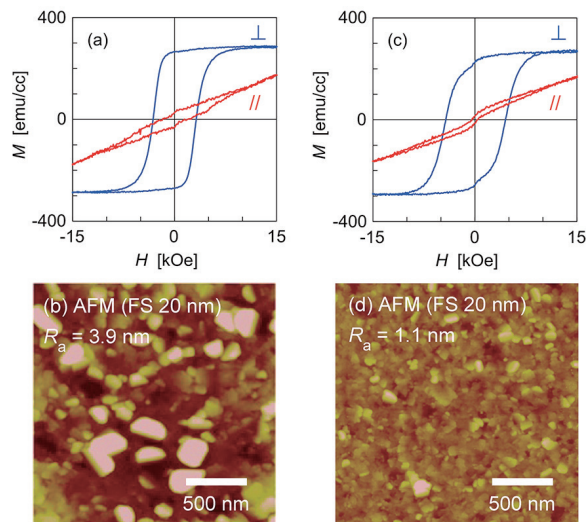
Fig. 6 (a), (c) *M-H* curves and (b), (d) AFM images with a full-scale (FS) 20 nm of ultrathin MnGa films on a Si substrate. The films were grown on (a), (c) a CoGa and (b), (d) Cr layer. The CoGa layer was sputter-deposited at $T_s^{CoGa} = 400$ °C and annealed at $T_a^{CoGa} = 700$ °C.

dependence of the lattice constant *c* of the CoGa layer, which was calculated from the peak position of CoGa 001, since CoGa 002 and Cr 002 peaks were overlapped. The lattice constant of the CoGa layer became close to that of a bulk CoGa[19] ($a = 0.2877$ nm) with increasing T_s^{CoGa} up to 400 °C, as shown in Fig. 3(b). This result may be one of the reasons for the increase of M_s with increasing T_s^{CoGa} up to 400 °C. Further increase of T_s^{CoGa} caused significant increase in the roughness of the CoGa surface, as shown in Fig. 2, which might inhibit growth of the (001)-oriented L1$_0$-MnGa layer.

Hereafter, T_s^{CoGa} was fixed to be 400 °C, and the post-annealing temperature of the CoGa layer T_a^{CoGa} was varied from 500–800 °C. Figure 4 shows T_a^{CoGa} dependence of M_s and R_a of ultrathin MnGa films on Si substrates. M_s reached maximum value at $T_a^{CoGa} = 700$ °C, while R_a increased with increasing T_a^{CoGa}. The increase in R_a is considered to be due to the increase of the surface roughness of the CoGa layer with increasing T_a^{CoGa}, because CoGa films without MnGa layers annealed at 700 °C exhibited large R_a (not shown here). Figure 5 shows XRD patterns of ultrathin MnGa films on Si substrates using CoGa buffer layers. The CoGa layer was deposited at $T_s^{CoGa} = 400$ °C, and the post-annealing temperature T_a^{CoGa} was varied from 500–800 °C. Similar to Fig. 3(a), the samples prepared at up to $T_a^{CoGa} = 700$ °C show (001)-oriented growth of the CoGa, Cr, and MgO layers. At $T_a^{CoGa} = 800$ °C, CoGa 001 and 002 and Cr 002 peaks disappeared, which may have been due to the alloying of CoGa and Cr. The variation in the crystal structure of the CoGa layer may have resulted in increased CoGa surface roughness. For the samples prepared at $T_a^{CoGa} = 600$ °C and 700 °C, the MnGa 002 peak was visible around $2\theta = 53$°, which is

higher than the angle estimated in a bulk MnGa (dashed line). This suggests that the MnGa lattice was compressed along the [001] direction and expanded in plane to decrease the lattice mismatch between MnGa and CoGa. The appearance of the MnGa 002 peak is considered to reflect the formation of (001)-oriented L1$_0$-MnGa, and to be related to the increase of M_s, as seen in Fig. 4.

As discussed above, the M_s of the MnGa layer estimated from the hysteresis loop along the film normal direction was increased with increasing T_s^{CoGa} up to a certain temperature, and then abruptly disappeared. In the present film stack, the rather high annealing temperature of $T_a^{CoGa} = 700$ °C was effective in promoting the crystal growth of the MnGa layer. This post-annealing temperature was much higher than those for the CoGa buffer layer on the MgO single crystal substrate (see Fig. 1). Such a high annealing temperature was also necessary in the MnGa film grown on the Si substrate with Cr buffer layer[13].

Figure 6 shows (a) out-of-plane and in-plane *M-H* curves, and (b) an AFM image of the ultrathin MnGa film grown on the Si substrate using the CoGa buffer layer with $T_s^{CoGa} = 400$ °C and $T_a^{CoGa} = 700$ °C (optimum condition in the present study). As a reference, *M-H* curves and an AFM image of the MnGa film grown on a Cr layer are shown in Figs. 6 (c) and (d), respectively. M_s of the MnGa films on the CoGa and Cr layers were 290 and 280 emu/cc, respectively, which were almost the same as that on the MgO substrate shown in Fig. 1(a). The squareness of the out-of-plane *M-H* curve increased and the coercivity decreased by inserting the CoGa layer on the Cr layer, which suggests the (001) orientation and continuity of the MnGa layer were improved compared to our previous study. However, R_a of the film with the CoGa layer was 3.9 nm, greater than that of the MnGa film grown on the Cr layer. This may have been due to the rough surface of the CoGa buffer layer, and improvement of the surface roughness is necessary for the application to HDD. Further study of the composition and annealing conditions of the CoGa layer, such as rapid thermal annealing, should be investigated.

4. Conclusion

Ultrathin MnGa films on thermally oxidized Si substrates were fabricated by inserting a CoGa buffer layer, and the growth conditions of the CoGa buffer layer were investigated to obtain MnGa film with a large saturation magnetization. In the MnGa film on the Si substrate, saturation magnetization of 290 emu/cc was obtained when the CoGa buffer layer was sputter-deposited at 400 °C and post-annealed at 700 °C. The saturation magnetization of the MnGa film on the Si substrate was almost the same with that on the MgO substrate. The hysteresis loop of the MnGa film exhibited almost unity squareness and low coercivity by the insertion of the CoGa buffer layer, suggesting the

improvement of (001) orientation and continuity of the MnGa layer. However, the post-annealing of the CoGa layer at high temperature resulted in increased surface roughness. Improvement of the surface roughness is necessary for practical application to BPM.

References

1) The International Disk Drive Equipment and Materials Association, "ASTC Technology Roadmap", 2016.
2) A. Kikitsu, Y. Kamata, M. Sakurai, and K. Naito: *IEEE Trans. Magn.*, **43**, pp.3685-3688 (2007).
3) C. Chappert, H. Bernas, J. Ferré, V. Kottler, J.-P. Jamet, Y. Chen, E. Cambril, T. Devolder, F. Rousseaux, V. Mathet, and H. Launois: *Science*, **280**, pp.1919-1922 (1998).
4) B. D. Terris, L. Folks, D. Weller, J. E. E. Baglin, J. Kellock, H. Rothuizen, and P. Vettiger: *Appl. Phys. Lett.*, **75**, pp.403-405 (1999).
5) J. Ferré, C. Chappert, H. Bernas, J.-P. Jamet, P. Meyer, O. Kaitasov, S. Lemerle, V. Mathet, F. Rousseaux, and H. Launois: *J. Magn. Magn. Mat.*, **198–199**, pp.191-193 (1999).
6) R. Hyndman, P. Warin, J. Gierak, J. Ferré, J. N. Chapman, J. -P. Jamet, V. Mathet, and C. Chappert: *J. Appl. Phys.*, **90**, pp.3843-3849 (2001).
7) E. Suharyadi, S. Natsume, T. Kato, S. Tsunashima, and S. Iwata: *IEEE Trans. Magn.*, **41**, pp.3595-3597 (2005).
8) E. Suharyadi, T. Kato, S. Tsunashima, and S. Iwata: *IEEE Trans. Magn.*, **42**, pp.2972-2974 (2006).
9) D. Oshima, M. Tanimoto, T. Kato, Y. Fujiwara, T. Nakamura, Y. Kotani, S. Tsunashima, and S. Iwata: *IEEE Trans. Magn.*, **50**, 3203407 (2014).
10) T. Kato, S, Iwata, Y. Yamauchi, and S. Tsunashima: *J. Appl. Phys.*, **106**, 053908 (2009).
11) Q. Xu, R. Kanbara, T. Kato, S. Iwata, and S. Tsunashima: *J. Appl. Phys.*, **111**, 07B906 (2012).
12) D. Oshima, T. Kato, S. Iwata, and S. Tsunashima: *IEEE Trans. Magn.*, **49**, pp.3608-3611 (2013).
13) D. Oshima, T. Kato, and S. Iwata: *IEEE Trans. Magn.*, **54**, 3200207 (2018).
14) T. Ishikawa, Y. Miwa, D. Oshima, T. Kato, and S. Iwata: *IEEE Trans. Magn.*, **55**, 3200104 (2019).
15) T. Kato, D. Oshima, and S. Iwata: *Crystals*, **9**, 27 (2018).
16) Y. Takahashi, H. Makuta, T. Shima, and M. Doi: *T. Magn. Soc. Jpn.* (Special Issues), **1**, pp. 30-33 (2017).
17) K. Z. Suzuki, R. Ranjbar, A. Sugihara, T. Miyazaki, and S. Mizukami: *Jpn. J. Appl. Phys.*, **55**, 010305 (2016).
18) J. Wang, Y. K. Takahashi, K. Yakushiji, H. Sepehri-Amin, H. Kubota, and K. Hono: *61st Annual Conference on Magnetism and Magnetic Materials*, HH-07 (2016).
19) H. Ipser, A. Mikula, and W. Schuster: Mon. für Chem., 120, p.283 (1989).

<Paper>

Media Design
for Three-Dimensional Heat-Assisted Magnetic Recording

T. Kobayashi, Y. Nakatani*, and Y. Fujiwara

Graduate School of Engineering, Mie Univ., *1577 Kurimamachiya-cho, Tsu 514-8507, Japan*

*Graduate School of Informatics and Engineering, Univ. of Electro-Communications, *1-5-1 Chofugaoka, Chofu 182-8585, Japan*

We design media for three-dimensional heat-assisted magnetic recording at 2 Tbpsi (total density of 4 Tbpsi), taking account of heat transfer simulation, field calculation, and information stability in high Curie temperature (HC) and low Curie temperature (LC) layers. The medium surface temperature while writing in the HC layer, the thermal gradients while writing in the HC and LC layers, and the grain temperature difference between the HC and LC layers while writing in the LC layer are discussed by using a heat transfer simulation. The magnetic field strength as a function of distance from the layer surface for a single layer is discussed by employing a field calculation. The Curie temperatures of T_{LC} and T_{HC}, and the grain heights of h_{LC} and h_{HC} in the LC and HC layers, respectively, are also discussed in terms of information stability during 10 years of archiving and writing in the LC layer. As a result, a media structure is decided whereby the upper, namely, the surface layer is an LC layer with T_{LC} = 625 K and h_{LC} = 4.5 nm, and the lower layer is an HC layer with T_{HC} = 750 K and h_{HC} = 6.0 nm with an anisotropy constant ratio of 0.8.

Key words: 3D HAMR, heat transfer simulation, field calculation, information stability

1. Introduction

Heat-assisted magnetic recording (HAMR) is a promising candidate as a next generation magnetic recording method capable of operating beyond the trilemma limit[1]. HAMR is a recording technique where the medium is heated to reduce coercivity during the writing period.

Three-dimensional magnetic recording is useful for increasing the recording capacity. Three-dimensional HAMR (3D HAMR) has been proposed[2] where the medium consists of a high Curie temperature T_{HC} (HC) layer and a low Curie temperature T_{LC} (LC) layer with no exchange coupling between the HC and LC layers. With 3D HAMR, once data have been written in the HC layer, other data can be written in the LC layer by employing lower temperature heating.

We have previously discussed the stability of the information in the HC layer while writing is under way in the LC layer, and the information stability in the HC and LC layers for 10 years of archiving[3]. This result was obtained under the assumptions that the temperatures in the HC and LC layers are the same, and that the thermal gradient for the cross-track direction is constant. However, the two layers have different temperatures and thermal gradients.

Furthermore, the magnetic field strength from the HC and LC layers is also important as regards readout.

In this paper, we design the 3D HAMR media at 2 Tbpsi (total density of 4 Tbpsi), while taking account of a heat transfer simulation, a field calculation, and the information stability in the HC and LC layers.

2. Calculation Method

2.1 Heat transfer simulation

We assumed the medium to be granular. The temperature profile for 3D HAMR depends on the materials between the grains and between the HC and LC layers. Suitable intergrain and interlayer materials are currently unknown. However, it is important to obtain the characteristics of the temperature profile in 3D HAMR. Therefore, we analytically estimated the temperature profile for the cross-track direction y using data published in previous papers 4) and 5) employing Eq. (1)

$$\frac{T_2(y) - T_{amb}}{T_1(y) - T_{amb}} = \frac{P_{w2}}{P_{w1}}, \qquad (1)$$

where $T_i(y)$ is the temperature for a heating power P_{wi}. The ambient temperature T_{amb} is the maximum working temperature of the hard drive, and is assumed to be 330 K. The temperature increase above the ambient temperature $T_i(y) - T_{amb}$ is proportional to P_{wi}.

Figure 1 shows a schematic illustration of the structure of a medium that consists of four layers, namely a recording layer (RL) (FePt base, HC 4 nm + LC 4 nm = 8 nm), interlayer 1 (IL1) (MgO base, 5 nm), interlayer 2 (IL2) (Cr base, 10 nm), and a heat-sink layer (Cu base, 30 nm). IL1 is a layer for c-axis orientation control of RL, and IL2 is a seed layer for IL1. There is no intergrain material and no interlayer material between the HC and LC layers. The x, y, and z axes are the down-track, the cross-track, and the film normal direction, respectively, where $y = 0$ at the track center and $z = 0$ at the RL surface. We focused on the medium surface temperature T_{surf} while

writing in the HC layer, the thermal gradients $\partial T / \partial y$ for the cross-track direction while writing in the HC and LC layers, and the grain temperature difference ΔT_{HL} at the track edges between the HC and LC layers while writing in the LC layer.

The thermal constants are summarized in Table 1. Two thermal conductivities of 50 and 4 W/(mK) were used for IL1.
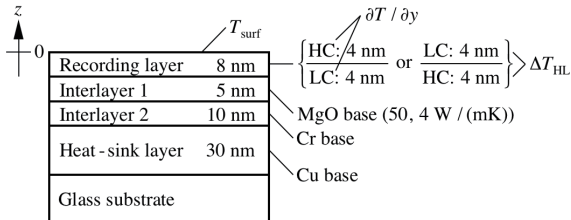

Fig. 1 Film structure for heat transfer simulation.

Table 1 Thermal constants for heat transfer simulation.

	Specific heat	Thermal conductivity
Recording layer	200 J / (kgK) 3 J / (cm^{3}K)	100 W / (mK)
Interlayer 1	500 J / (kgK) 2 J / (cm^{3}K)	50, 4 W / (mK)
Interlayer 2	360 J / (kgK) 2.5 J / (cm^{3}K)	100 W / (mK)
Heat - sink layer	440 J / (kgK) 4 J / (cm^{3}K)	400 W / (mK)
Glass substrate	1000 J / (kgK) 2 J / (cm^{3}K)	1 W / (mK)

2.2 Field calculation

The magnetic field strength from the upper and lower layers, as shown in Fig. 2, was calculated using an analytical equation. One bit has 3 grains for the down-track direction and 3 grains for the cross-track direction, namely, there are 9 grains/bit. The bit aspect ratio is one. The grain size D_m and the intergrain spacing Δ_G are 5.0 nm and 1 nm, respectively, with no grain size distribution. The flying height h_{fly} is the distance between the magnetic head reader and the upper layer surface. The grain heights and the magnetizations for the upper and lower layers are h_U, h_L, M_{sU}, and M_{sL}, respectively.

The interlayer spacing Δ_L for suppressing the exchange coupling between the upper and lower layers strongly depends on the interlayer material. And Δ_L should be thinner due to the higher field strength at the reader from the lower layer. On the assumption that we had selected an appropriate material, we chose a Δ_L value of 1 nm.
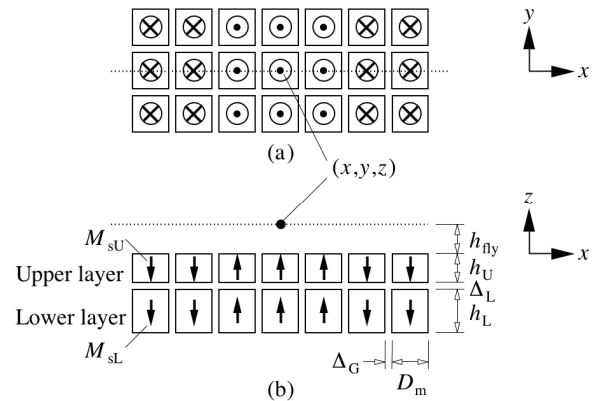

Fig. 2 Grain arrangement for field calculation. (a) Top and (b) side views.

2.3 Information stability

The bit error rate (bER) for estimating information stability was calculated using the grain error probability[3], taking account of the shape anisotropy $M_s H_d / 2$ using a self-demagnetizing field H_d as shown in Fig. 3. The temperature dependence of the magnetic properties was determined by performing a mean field analysis[3].

The conditions used when calculating the information stability in the HC and LC layers are summarized in Table 2.

We assumed that the grain size distribution was log-normal with a mean grain size D_m of 5.0 nm and a standard deviation σ_D / D_m of 15 %.

The temperature in the center of the track while writing is higher than that at the track boundary by $(\partial T / \partial y) \cdot (D_T / 2)$ where D_T is the track width. Therefore, the temperature of the writing head and the surface lubricant while writing in the HC layer decreases as D_T, namely the bit aspect ratio D_T / D_B, decreases[5]. And the peak temperature while writing in the LC layer also decreases as D_T / D_B decreases as shown in Fig. 4. Furthermore, increasing the grain column number per bit, namely, decreasing D_T / D_B, is effective in reducing the bER caused by the Curie temperature T_c variation[6]. Therefore, we chose a D_T / D_B value of 1.

We have introduced an HAMR design parameter, namely, the medium anisotropy constant ratio K_u / K_{bulk} [4], in place of the medium anisotropy constant K_u since the K_u value is a function of the medium T_c. K_u / K_{bulk} is the intrinsic ratio of the medium K_u to bulk FePt K_u regardless of T_c where FePt is a candidate HAMR medium material thanks to its high K_u and relatively low T_c. Although a low T_c is advantageous for writing in HAMR, a higher K_u / K_{bulk} is needed for a low T_c medium for 10 years of archiving[7], and a medium with a high K_u / K_{bulk}, e.g. 0.6 − 1.0, is difficult to manufacture regardless of T_c[8]. And then, a high K_u / K_{bulk} must be achieved in 3D HAMR to realize information stability in the HC layer

while writing in the LC layer, and to realize information stability in the LC layer during 10 years of archiving[3]. The K_u / K_{bulk} value was revised to 0.8 from 0.85 or 0.86 in a previous paper[3] since the value of 0.85 appears to be too high for manufacturing a medium.

We also assumed that the T_c distribution was normal with a mean Curie temperature T_{cm} and a standard deviation σ_{Tc} / T_{cm} of 2 %. No intrinsic distribution of K_u was assumed. However, there was a fluctuation in K_u caused by σ_{Tc}.

The temperature profile for the cross-track direction while writing in the LC layer[3] was also revised, and that used in this paper is shown in Fig. 4. The LC writing temperature of the grains at the track edges was assumed to be $T_{LC} + 2\sigma_{TLC}$, taking account of the standard deviation σ_{TLC} of T_{LC}. The LC writing temperature of the grain in the center of the track was assumed to be

$$T_{LC} + 2\sigma_{TLC} + \frac{\partial T}{\partial y}(D_m + \Delta_G), \qquad (2)$$

taking account of $\partial T / \partial y$ = 10 K/nm.

Fig. 3 Self-demagnetizing field H_d for grains with magnetization M_s and volume $D \times D \times h$ where D and h are grain size and height, respectively.

Table 2 Calculation conditions.

Recording density (Tbpsi)	2
Total density (Tbpsi)	4
Gilbert damping constant α	0.1
Grain number $m \times n$ (grains / bit)	3×3
Intergrain spacing Δ_G (nm)	1
Mean grain size D_m (nm)	5.0
Standard deviation σ_D / D_m (%) of D_m	15
Bit pitch D_B (nm)	18.0
Track width D_T (nm)	18.0
Bit aspect ratio D_T / D_B	1
Anisotropy constant ratio K_u / K_{bulk}	0.8
Standard deviation σ_{Tc} / T_{cm} (%) of T_{cm}	2
Thermal gradient $\partial T / \partial y$ (K / nm)	10
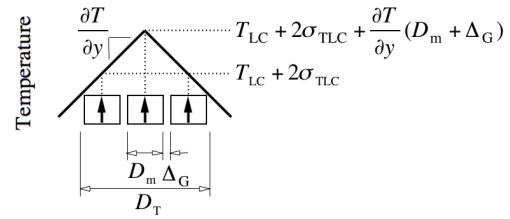
Fig. 4 Temperature profile for information stability in HC layer while writing in LC layer.

3. Calculation Results

3.1 Heat transfer simulation

The writing temperature of the grains at the track edges was assumed to be $T_{cm} + 2\sigma_{Tc}$ for the HC and LC layers where T_{cm} and σ_{Tc} are the mean Curie temperature and the standard deviation of T_{cm}, respectively, taking account of the Curie temperature variation.

Figure 5 shows the temperature profiles for the cross-track direction where we used an interlayer 1 (IL1) thermal conductivity of 50 W/(mK) and an HC (upper, namely, surface, T_{HC} = 750 K) / LC (lower, T_{LC} = 550 K) layer structure. The solid lines indicate the temperatures at the layer boundaries, and the dotted lines indicate those at the layer centers.
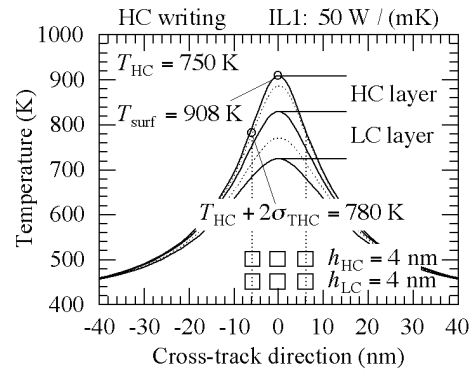
(a) $\partial T_H / \partial y$ = 25.2 K/nm
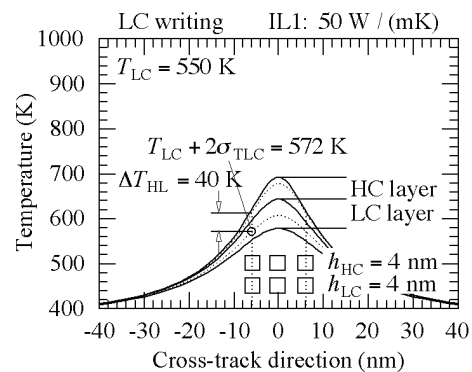
(b) $\partial T_L / \partial y$ = 9.5 K/nm
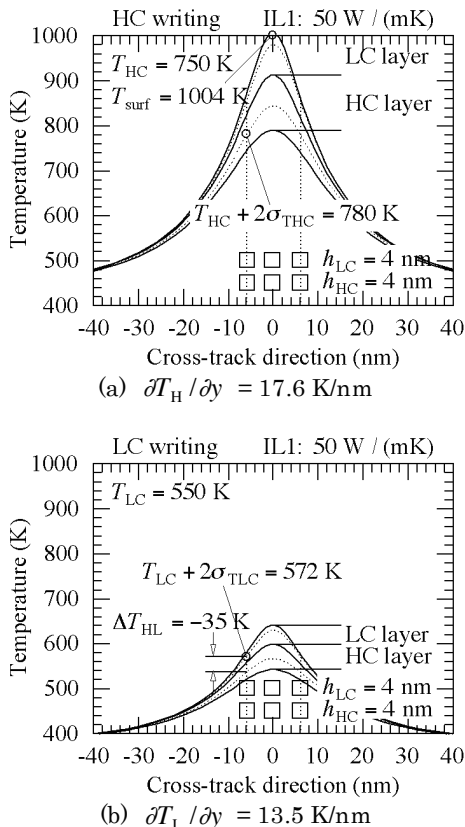
Fig. 5 Temperature profile for the cross-track direction for an IL1 thermal conductivity of 50 W/(mK) and an HC (upper) / LC (lower) layer structure while writing in the (a) HC and (b) LC layers.

(a) When writing in the HC layer (HC writing), the temperature at $y = \pm 6$ nm and $z = -2$ nm is $T_{HC} + 2\sigma_{THC} = 780$ K at which $\partial T_H / \partial y$ is 25.2 K/nm. The T_{surf} value is 908 K.

(b) When writing in the LC layer (LC writing), the temperature at $y = \pm 6$ nm and $z = -6$ nm is $T_{LC} + 2\sigma_{TLC} = 572$ K at which $\partial T_L / \partial y$ is 9.5 K/nm. The ΔT_{HL} value is 40 K.

On the other hand, Fig. 6 shows the temperature profiles for the cross-track direction where the LC (upper) / HC (lower) layer structure is used.

(a) When HC writing, the temperature at $y = \pm 6$ nm and $z = -6$ nm is $T_{HC} + 2\sigma_{THC} = 780$ K at which $\partial T_H / \partial y$ is 17.6 K/nm. The T_{surf} value is 1004 K.

(b) When LC writing, the temperature at $y = \pm 6$ nm and $z = -2$ nm is $T_{LC} + 2\sigma_{TLC} = 572$ K at which $\partial T_L / \partial y$ is 13.5 K/nm. The ΔT_{HL} value is -35 K.

The T_{surf} value of 1004 K for LC / HC in Fig. 6 (a) is higher than that of 908 K for HC / LC in Fig. 5 (a) since HC is the lower layer.

The $\partial T / \partial y$ value of 25.2 K/nm for the HC / LC structure and the upper HC writing in Fig. 5 (a) is higher than that of 13.5 K/nm for LC / HC and the upper LC writing in Fig. 6 (b) due to their Curie temperatures.

(a) $\partial T_H / \partial y = 17.6$ K/nm

(b) $\partial T_L / \partial y = 13.5$ K/nm

Fig. 6 Temperature profile for the cross-track direction for an IL1 thermal conductivity of 50 W/(mK) and an LC / HC layer structure while writing in the (a) HC and (b) LC layers.

Employing Eq. (1), we find that the thermal gradient $\partial T_H / \partial y$ for the HC layer at the track edges is intrinsically larger than $\partial T_L / \partial y$ for the LC layer as shown in Eq. (3),

$$\frac{T_H(y) - T_{amb}}{T_L(y) - T_{amb}} = \frac{T_H(\pm 6 \text{ nm}) - T_{amb}}{T_L(\pm 6 \text{ nm}) - T_{amb}} = \frac{T_{HC} + 2\sigma_{THC} - T_{amb}}{T_{LC} + 2\sigma_{TLC} - T_{amb}},$$

$$T_H(y) - T_{amb} = \frac{T_{HC} + 2\sigma_{THC} - T_{amb}}{T_{LC} + 2\sigma_{TLC} - T_{amb}}(T_L(y) - T_{amb}),$$

$$\therefore \frac{\partial T_H(y)}{\partial y} = \frac{T_{HC} + 2\sigma_{THC} - T_{amb}}{T_{LC} + 2\sigma_{TLC} - T_{amb}} \cdot \frac{\partial T_L(y)}{\partial y}. \quad (3)$$

And then, the $\partial T_H / \partial y$ of 25.2 K/nm for HC / LC structure and the upper HC writing in Fig. 5 (a) is higher than that of 17.6 K/nm for LC / HC and the lower HC writing in Fig. 6 (a) due to a heat flow in the in-plane direction at the depths of the layer.

Therefore, the thermal gradient has the following characteristics:
(1) The thermal gradient for the HC layer is intrinsically larger than that for the LC layer due to their respective Curie temperatures.
(2) The thermal gradient for the upper layer is intrinsically larger than that for the lower layer due to a heat flow.

These two characteristics are very important in 3D HAMR.

The $\partial T_H / \partial y$ of 25.2 K/nm for the HC / LC structure and HC writing in Fig. 5 (a) is relatively large due to the combination of the HC layer and the upper layer. And the $\partial T_L / \partial y$ of 9.5 K/nm for the HC / LC structure and LC writing in Fig. 5 (b) is relatively small due to the combination of the LC layer and the lower layer.

On the other hand, for the LC / HC structure, the difference between the $\partial T / \partial y$ values of 17.6 K/nm for HC writing and 13.5 K/nm for LC writing in Fig. 6 is small due to the opposite combinations.

If $\partial T / \partial y$ is small, the information in tracks adjacent to the writing track becomes unstable. Furthermore, $\partial T / \partial y$ and $\partial T / \partial x$ are almost the same for the cross-track and down-track directions, respectively[4]. If $\partial T / \partial x$ is too large, the writing temperature decreases before writing, and write-error increases. If $\partial T / \partial x$ is too small, it is difficult to reduce the writing temperature, and the magnetization is reversed by the reversed writing field when writing the next bit. Then, erasure-after-write increases. Therefore, the small difference in the $\partial T / \partial x$ values for HC and LC writing is preferable in terms of the writing property[8].

When the ΔT_{HL} value is negative, the temperature in the HC layer while writing in the LC layer is lower than that in the LC layer, and this is advantageous in relation to the information stability in the HC layer. And the ΔT_{HL} value of -35 K for the LC / HC structure in Fig. 6 (b) is negative since HC is the lower layer.
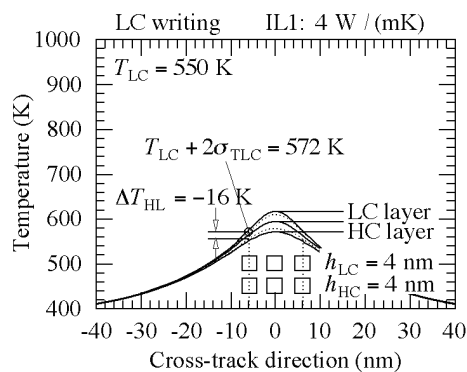
The results obtained for the IL1 thermal conductivity of 50 W/(mK) are summarized in Table 3. Although the T_{surf} value is high, an LC (upper) / HC (lower) layer structure is preferable as regards $\partial T / \partial y$ and ΔT_{HL}.

Table 3 Results of heat transfer simulation (thermal conductivity of interlayer 1 (IL1): 50 W/(mK)).

IL1: 50 W / (mK)	HC writing	LC writing
HC layer / LC layer		
T_{cm} (K)	750	550
T_{surf} (K)	908	
$\partial T / \partial y$ (K / nm)	25.2	9.5
ΔT_{HL} (K)		40
LC layer / HC layer		
T_{cm} (K)	750	550
T_{surf} (K)	1004	
$\partial T / \partial y$ (K / nm)	17.6	13.5
ΔT_{HL} (K)		−35
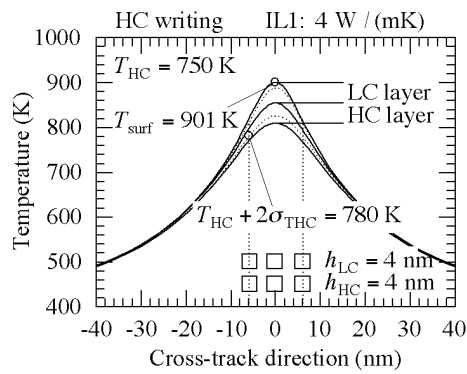
(a) $\partial T_{\mathrm{H}} / \partial y = 13.0$ K/nm

(b) $\partial T_{\mathrm{L}} / \partial y = 9.4$ K/nm

Fig. 7 Temperature profile for the cross-track direction for an IL1 thermal conductivity of 4 W/(mK) and an LC / HC layer structure while writing in the (a) HC and (b) LC layers.

The results for the IL1 thermal conductivity of 4 W/(mK) are shown in Fig. 7 and summarized in Table 4. The temperature difference between the HC and LC

layers for 4 W/(mK) in Fig. 7 is lower than that for 50 W/(mK) in Fig. 6 since the heat flow perpendicular to the film plane was reduced by the adiabatic effect of IL1. Therefore, the T_{surf} values for 4 W/(mK) in Table 4 are lower than the corresponding values for 50 W/(mK) in Table 3. Although the T_{surf} values can be reduced, the $\partial T / \partial y$ values become small.

It should be noted that the temperature of the LC layer ($z = -2$ nm) in the center of adjacent tracks ($y = \pm 18$ nm) while writing in the HC layer is 635 K as shown in Fig. 7 (a), and HC writing will erase data in the adjacent tracks. Therefore, it is necessary to devise a writing method, *e.g.* combination with shingled magnetic recording.

In short, an LC (upper, namely, surface) / HC (lower) layer structure is preferable as regards $\partial T / \partial y$ and ΔT_{HL}. An adiabatic medium structure with a low thermal conductivity of IL1 is also preferable as regards T_{surf}.

Table 4 Results of heat transfer simulation (thermal conductivity of interlayer 1 (IL1): 4 W/(mK)).

IL1: 4 W / (mK)	HC writing	LC writing
HC layer / LC layer		
T_{cm} (K)	750	550
T_{surf} (K)	864	
$\partial T / \partial y$ (K / nm)	17.5	7.0
ΔT_{HL} (K)		17
LC layer / HC layer		
T_{cm} (K)	750	550
T_{surf} (K)	901	
$\partial T / \partial y$ (K / nm)	13.0	9.4
ΔT_{HL} (K)		−16

3.2 Field calculation

Figure 8 shows the peak z component H_{zpeak} of the magnetic field as a function of the distance from the layer surface for a single layer where M_{s} is 1000 emu/cm³. For the upper layer,

$$\text{Distance} = h_{\mathrm{fly}}, \qquad (4)$$

and for the lower layer,

$$\text{Distance} = h_{\mathrm{fly}} + h_{\mathrm{U}} + \Delta_{\mathrm{L}}. \qquad (5)$$

The dotted lines indicate fitting by an exponential function.

The H_{zpeak} value from the medium decreases exponentially with a distance of more than 3 nm. Therefore, a low h_{U} (thin upper layer) is preferable in terms of ensuring a high H_{zpeak} from the lower layer. On the other hand, increasing the grain height (layer thickness) is an effective way of increasing H_{zpeak} as shown in Fig. 9.

The temperature dependence of M_s was roughly estimated under the assumption of $M_s(T_c = 770 \text{ K}, T = 300 \text{ K}) = 1000 \text{ emu/cm}^3$ as shown in Fig. 10. $M_s(T_c, T)$ increases as T_c increases. The HC layer is preferable as the lower layer since it has a larger M_s.

In short, a thin LC (upper) / HC (lower) layer structure is preferable as regards H_{zpeak}.
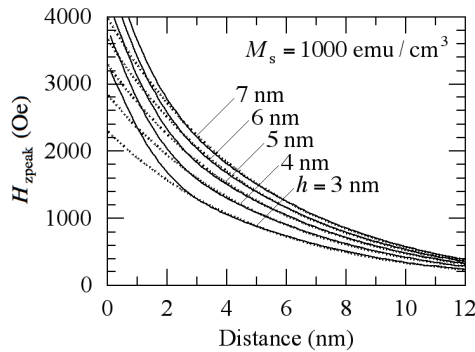

Fig. 8 Peak field strength H_{zpeak} as a function of distance from the layer surface for a single layer with grain height h.
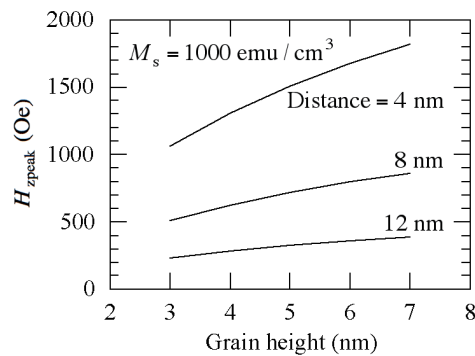
Fig. 9 Peak field strength H_{zpeak} as a function of grain height h for various distances.
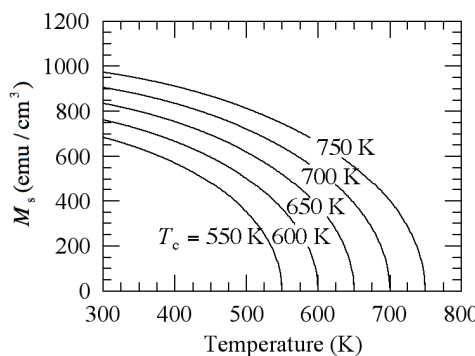
Fig. 10 Temperature dependence of magnetization M_s for various Curie temperatures T_c.

3.3 Information stability for 10 years of archiving

Next, we discuss a way of reducing the LC grain height (layer thickness) h_{LC}.

The h_{LC} value is limited by the information stability needed for 10 years of archiving. Figure 11 shows the

bit error rate (bER) as a function of the grain height h under the conditions of a T_{cm} of 550 K, no writing field H_w, a storage temperature T_{sto} of 350 K, and a storage time t_{sto} of 10 years. It can be seen that the grain height of 6.5 nm is necessary for bER = 1E−3. The required T_{cm} value for 10 years of archiving was obtained as a function of h with a bER of 1E−3 as shown in Fig. 12.

In short, the h_{LC} value can be reduced by increasing T_{LC} since K_u increases as T_c increases under a constant K_u/K_{bulk} [8].
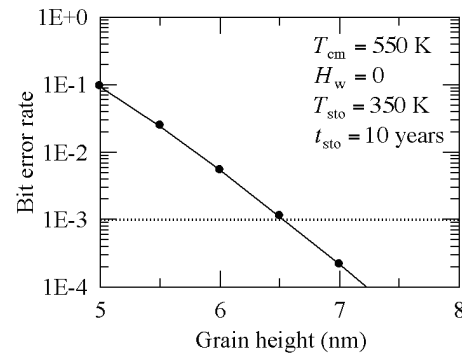
Fig. 11 Bit error rate necessary for 10 years of archiving as a function of grain height (layer thickness) h.
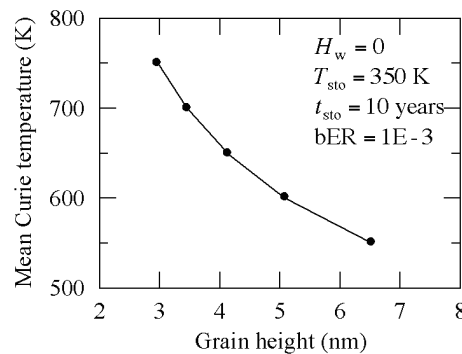
Fig. 12 Mean Curie temperature T_{cm} necessary for 10 years of archiving as a function of grain height (layer thickness) h.

3.4 Information stability in HC layer while writing in LC layer

The T_{LC} value is limited by the information stability in the HC layer while writing in the LC layer. The T_{HC} value required for the information stability was obtained as a function of T_{LC} for various HC grain heights (layer thicknesses) h_{HC} for a writing field H_w of −10 kOe, a time t of 1 nm, and a bER of 1E−4 as shown in Fig. 13. The dotted line indicates the limit for 10 years of archiving, taking account of the result in Fig. 12.

In short, the T_{LC} value can be raised by increasing T_{HC} and/or h_{HC}. However, increasing h_{HC} to more than 6 nm does not seem to be effective for increasing T_{LC} as shown in Fig. 14.
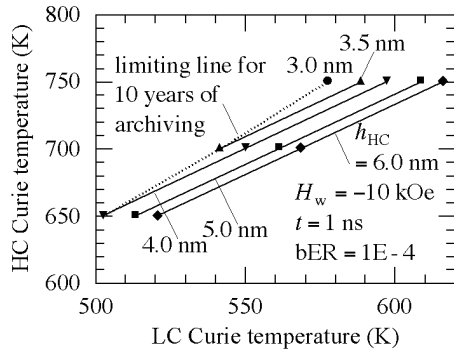
Fig. 13 HC Curie temperature T_{HC} required for information stability in the HC layer as a function of the LC Curie temperature T_{LC} for various HC grain heights (layer thicknesses) h_{HC}.
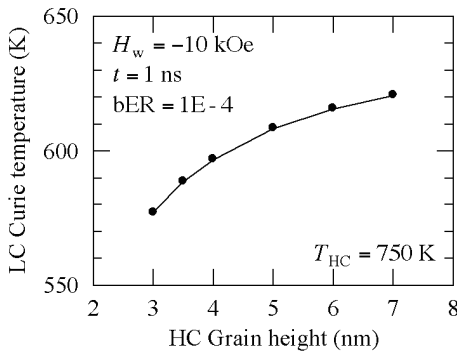

Fig. 14 T_{LC} required for information stability in the HC layer as a function of h_{HC} at $T_{HC} = 750$ K.

3.5 Layer design

Finally, we decided the layer structure for the 3D HAMR media as shown in Fig. 15 using the above results.

We assumed the upper layer to be the LC layer, and the lower layer to be the HC layer with $T_{HC} = 750$ K and $h_{HC} = 6.0$ nm, taking account of the results in **3.1**, **3.2**, and **3.4**. Then the LC layer has $T_{LC} = 625$ K and $h_{LC} = 4.5$ nm as a result, taking account of ΔT_{HL} in **3.1** and h in **3.3**, respectively.

Figure 16 shows the z component H_z of the magnetic field from the LC and HC layers for the down-track direction. The H_{zpeak} values are 1098 and 570 Oe from the LC and HC layers, respectively, where h_{fly} is 4.0 nm.
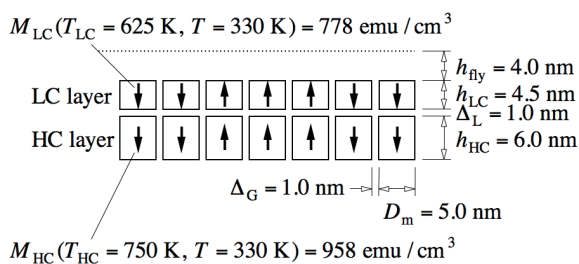
Fig. 15 Layer structure for 3D HAMR.
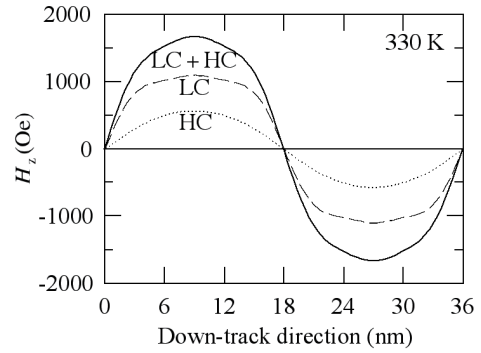
Fig. 16 Field strength H_z from LC and HC layers for the down-track direction.

4. Conclusions

We designed 3D HAMR media at 2 Tbpsi (total density of 4 Tbpsi), taking account of a heat transfer simulation, field calculation, and information stability in high Curie temperature (HC) and low Curie temperature (LC) layers.

(1) An LC (upper, namely, surface) / HC (lower) layer structure is preferable as regards the thermal gradients while writing in the HC and LC layers and information stability in the HC layer while writing in the LC layer. An adiabatic medium structure is also preferable as regards the surface temperature.

(2) A thin upper layer and a lower HC layer are preferable in terms of ensuring a high magnetic field from the lower layer.

(3) The LC grain height (layer thickness) h_{LC} can be reduced by increasing the LC Curie temperature T_{LC}.

(4) The T_{LC} value can be raised by increasing the HC Curie temperature T_{HC} and/or the HC grain height (layer thickness) h_{HC}.

We decided the layer structure for the 3D HAMR media using the above results. The upper layer is an LC layer with $T_{LC} = 625$ K and $h_{LC} = 4.5$ nm, and the lower layer is an HC layer with $T_{HC} = 750$ K and $h_{HC} = 6.0$ nm with an anisotropy constant ratio of 0.8.

References

1) S. H. Charap, P. -L. Lu, and Y. He: *IEEE Trans. Magn.*, **33**, 978 (1997).
2) Western Digital: private communication.
3) T. Kobayashi, Y. Nakatani, and Y. Fujiwara: *J. Magn. Soc. Jpn.*, **44**, 34 (2020).
4) T. Kobayashi, Y. Isowaki, and Y. Fujiwara: *J. Magn. Soc. Jpn.*, **39**, 8 (2015).
5) T. Kobayashi, Y. Isowaki, and Y. Fujiwara: *J. Magn. Soc. Jpn.*, **39**, 139 (2015).
6) T. Kobayashi, Y. Nakatani, and Y. Fujiwara: *J. Magn. Soc. Jpn.*, **43**, 70 (2019).
7) T. Kobayashi, Y. Nakatani, and Y. Fujiwara: *J. Magn. Soc. Jpn.*, **43**, 114 (2019).
8) T. Kobayashi, Y. Nakatani, and Y. Fujiwara: *J. Magn. Soc. Jpn.*, **42**, 110 (2018).

Notice for Photocopying

複写をされる方へ